AGU ADVANCING EARTH AND SPACE SCIENCE

Water Resources Research

RESEARCH ARTICLE
10.1029/2021WR030696

Lasting Effects of Soil Compaction on Soil Water Regime Confirmed by Geoelectrical Monitoring

Alejandro Romero-Ruiz[1], Niklas Linde[1], Ludovic Baron[1], Daniel Breitenstein[2], Thomas Keller[3,4], and Dani Or[2,5]

[1]Institute of Earth Sciences, University of Lausanne, Lausanne, Switzerland, [2]Institute of Biogeochemistry and Pollutant Dynamics, Soil and Terrestrial Environmental Physics, Swiss Federal Institute of Technology, Zürich, Switzerland, [3]Department of Soil and Environment, Swedish University of Agricultural Sciences, Uppsala, Sweden, [4]Department of Agroecology and Environment, Agroscope, Zürich, Switzerland, [5]Desert Research Institute, Division of Hydrologic Sciences, Reno, NV, USA

Key Points:

- Effects of soil compaction on soil hydraulic properties are reflected in soil water dynamics as seen by geoelectrical measurements
- Pedophysical model predictions linking soil structural traits with electrical resistivity are consistent with soil hydraulic models
- Soil compaction reduced both electrical resistivity and hydraulic conductivity and enhanced surface evaporation relative to uncompacted soil

Supporting Information:

Supporting Information may be found in the online version of this article.

Correspondence to:

A. Romero-Ruiz,
alejandro.romeroruiz@unil.ch

Citation:

Romero-Ruiz, A., Linde, N., Baron, L., Breitenstein, D., Keller, T., & Or, D. (2022). Lasting effects of soil compaction on soil water regime confirmed by geoelectrical monitoring. *Water Resources Research*, *58*, e2021WR030696. https://doi.org/10.1029/2021WR030696

Received 26 JUN 2021
Accepted 19 DEC 2021

Abstract Despite its importance for hydrological and ecological soil functioning, characterizing, and quantifying soil structure in the field remains a challenge. Traditional characterization of soil structure often relies on point measurements, more recently, we advanced the use of minimally invasive geophysical methods that operate at plot-field scales and provide information under natural conditions. In this study, we expand the application using geoelectrical and time-domain reflectometry (TDR) monitoring of soil water dynamics to infer impacts of compaction on soil structure and function. We developed a modeling scheme combining a new pedophysical model of soil electrical conductivity and a soil-structure-informed one-dimensional water flow and heat-transfer model. The model was used to interpret Direct Current (DC)-resistivity and TDR monitoring data in compacted soils at the Soil Structure Observatory (SSO) located in the vicinity of Zürich, Switzerland. We find that (1) soil compaction leads to a persistent decrease in soil electrical resistivity and (2) that compacted soils are typically drier than non-compacted soils during long drying events. The main decrease in electrical resistivity is attributed to decreasing macroporosity and increasing connectivity of soil aggregates due to compaction. Higher water losses in compacted soils are explained in terms of enhanced evaporation. Our work advances characterization of soil structure at the field scale with electrical methods by offering a physically based explanation of the impact of soil compaction on electrical properties and by interpreting DC-resistivity data in terms of soil water dynamics.

1. Introduction

Soil structure refers to the spatial arrangement and binding of soil constituents that develop in response to biological activity, seasonal cycles of wetting and drying, freezing and thawing, and anthropogenic activities (Dexter, 1988). Earthworms moving through the soil combined with decaying roots generate networks of biopores (Bottinelli et al., 2015; Oades, 1993) that have a strong impact on soil hydraulic properties and related soil ecological services (Gerke et al., 2010; Jarvis et al., 2016; Vereecken et al., 2007). The rigorous definition of soil structure remains elusive and despite the growing recognition of soil structure as a determinant agent affecting hydraulic processes at the landscape scale, current climate models used in Earth System Science typically rely on pedotransfer functions that consider soil texture only (Van Looy et al., 2017), thereby, overlooking the important impact of soil structure (Bonetti et al., 2021; Fatichi et al., 2020).

Characterizing soil structure at the field scale remains a challenge due to the traditional reliance of invasive point measurements offering limited prospects for studying soil structure over larger spatial scales relevant to land management. Romero-Ruiz et al. (2018) proposed using geophysical methods as a complement to such traditional techniques. Particularly, electrical methods offer a potential for monitoring effects of soil structure on soil water regimes that cannot be deduced from bulk soil properties (e.g., bulk density and total porosity). Electrical properties of porous materials are widely used for capturing and characterizing water flow under different conditions (Binley et al., 2015; Binley & Slater, 2020). There is extensive theoretical and empirical evidence demonstrating that electrical properties of soils are sensitive to the volumetric fractions and electrical properties of the soil constituents and their spatial arrangement (Bussian, 1983; Cosenza et al., 2009; Day-Lewis et al., 2017; Glover, 2009; Glover et al., 2000; Moysey & Liu, 2012). Electrical methods have been used extensively to quantify water content in soils (Doolittle & Brevik, 2014) and compaction states (Besson et al., 2013). There is also an

increasing usage of geoelectrical methods for agricultural applications (Garré et al., 2021). Recently, Blanchy et al. (2020) demonstrated the potential of electromagnetic induction (EMI) and DC-resistivity methods to monitor the impact of agricultural practices in terms of soil compaction and von Hebel et al. (2020) used EMI and drone-based multispectral methods to delineate agricultural management zones at larger scales. Despite the accumulated wealth of studies relating soil electrical properties to various soil properties and states, providing a physically based description of how soil structure impacts electrical resistivity remains an open question.

We hypothesize that differences in the electrical resistivity of soils with different structure are influenced by: (1) direct effects of arrangement and volumetric fractions of soil constituents; (2) indirect effects on soil water dynamics (e.g., rapid versus slow infiltration and drainage, surface evaporation). We focus here on modifications to soil structure induced by vehicular compaction. Soil compaction is a common modifier of soil structure that adversely impacts soil functioning and its water regime (Hamza & Anderson, 2005). Disentangling effects of soil compaction on geoelectrical signatures is challenging due to its multiple effects on pore geometry, pore connectivity and its role in determining the volumetric proportion of the conducting liquid phase. Soil compaction reduces the capacity of the soil to provide water and oxygen to plant roots. It produces a reduction and disruption of the soil pore system (particularly biopores), which leads to a reduction in soil transport properties, impacts soil evaporation (Assouline et al., 2014), and decreases soil surface water infiltration. The effect of soil compaction on soil mechanical properties limits the ability of plant roots to reach larger soil volumes and extract water (Bengough et al., 2011). All these interacting processes ultimately determine the resulting soil water dynamics. Coupled hydrogeophysical modeling (e.g., Kowalsky et al., 2004) may enhance our quantitative understanding of the influence of soil structure on such natural processes and their corresponding effect on soil water dynamics and related geoelectrical signals. To advance our understanding of soil compaction effects on electrical resistivity and to disentangle compaction-induced effects of water content for improved monitoring capabilities, this work proposes a soil structure-based integrative modeling framework, that accounts for soil structure effects on soil electrical and hydraulic properties in a consistent manner, and their role in controlling soil processes impacting soil water dynamics.

Specifically, we seek to elucidate how geoelectrical monitoring can provide direct (via volumetric portions and arrangement of constituents) and indirect (via impact on soil water dynamics) information regarding soil structure. We employ a coupled hydrogeophysical modeling scheme to predict the primary signatures of soil structure on soil water dynamics and resulting geoelectrical properties. At its core, the modeling framework relies on a unified description of how compaction-induced changes on soil structure modify (1) the electrical resistivity, (2) the hydraulic conductivity function, and (3) the evaporation characteristics of the soil. To achieve this, we introduce a new pedophysical model of electrical properties based on a conceptualization of structured soils. We further infuse knowledge of how soil structure influences soil water retention and transport properties and how they control soil evaporation. The resulting transport, retention, and evaporation properties are incorporated in a one-dimensional water flow and heat-transfer model. This modeling framework is used to reproduce and interpret data from the Soil Structure Observatory (SSO) located in the vicinity of Zürich, Switzerland. We analyze four different experimental plots (combinations of two compaction treatments and two soil covers) presenting different water dynamics and geoelectrical responses but sharing the same soil texture. A qualitative description of precompaction and postcompaction signatures in geoelectrical data at the SSO can be found in Keller et al. (2017). Romero-Ruiz et al. (2021) provides a pedophysical model of soil elastic properties for interpreting monitored seismic signatures of compacted soils at the SSO. Additional ground-penetrating and DC-resistivity data are briefly discussed by Romero-Ruiz et al. (2018). Other nongeophysical studies at the SSO can be found in Colombi et al. (2017), Meurer et al. (2020), and Keller et al. (2021).

2. Soil-Structure-Informed Hydrogeophysical Modeling

Our coupled hydrogeophysical modeling scheme relies on a new pedophysical model of soil structure effects on bulk electrical properties that is conceptualized similarly to the modeling frameworks employed to predict hydraulic conductivity and soil evaporation. The pedophysical model is incorporated within a 1D modeling scheme of water flow and heat transfer in a layered soil profile. The hydraulic conductivity model accounts for macropore water flow (Durner, 1994) and the soil structure-specific evaporation properties are derived from water retention and transport properties (e.g., van Genuchten, 1980) using the model by Lehmann et al. (2020). We convert modeled time series of water content to soil relative permittivity for comparison with Time-Domain Reflectometry

(TDR) measurements of soil dielectric constant. Our pedophysical model is used to calculate electrical conductivity profiles from soil properties, water content, and temperature profiles resulting from the water flow and heat-transfer simulations. The electrical conductivity profiles are then used to calculate apparent electrical resistivity for comparison with measured data. Subsequently, a Markov-chain Monte Carlo (MCMC) method is used to infer posterior probability density functions of the unknown geoelectrical parameters of interest.

2.1. Pedophysical Model of Electrical Conductivity of Structured Soil

The electrical conductivities are modeled with a new pedophysical model that accounts for the arrangement of soil constituents. The soil electrical conductivity is predicted by considering the combined impact of the soil matrix (represented by an assembly of soil aggregates) and soil macropores. Similar conceptualizations have been successfully used to compute electrical (Day-Lewis et al., 2017), seismic (Dvorkin et al., 1999; Romero-Ruiz et al., 2021), and dielectric (Blonquist et al., 2006) properties of structured porous media. The soil matrix is composed by a water-air fluid mixture containing soil grains inclusions, while the macroporous region is composed by a water-air fluid mixture. The total porosity (ϕ_T, $cm^3\ cm^{-3}$) is expressed as a function of the soil matrix porosity (ϕ_{sm}, $cm^3\ cm^{-3}$) and the macroporous region ($\phi_{mac} = 1 cm^3\ cm^{-3}$) together with the volumetric fraction occupied by the soil macropores (w_{mac}, $cm^3\ cm^{-3}$) and the soil matrix ($1 - w_{mac}$):

$$\phi_T = (1 - w_{mac})\phi_{sm} + w_{mac}\phi_{mac}. \tag{1}$$

The predicted electrical conductivity is obtained by applying three mixing steps (Figure 1a) to derive: (1) the electrical conductivity of the partially saturated soil matrix, (2) the electrical conductivity of the partially saturated macropores, and (3) the electrical conductivity of the structured soil (soil matrix with embedded macropores).

The electrical conductivity of the soil matrix (σ_{sm}, S/m) considers surface conductivity (σ_s, S/m) that is prominent in fine textured soils (e.g., agricultural soils; Friedman, 2005). Surface conductivity is often accounted for by considering that electrical pathways are determined by the pore geometry (i.e., the high salinity limit; Linde et al., 2006; Waxman & Smits, 1968). Despite such restrictive assumptions, these models are widely used in soil science and hydrogeophysics (Linde et al., 2006; Seladji et al., 2010; Tran et al., 2017). Here, we account for surface conductivity in a more general manner by using Differential Effective Medium theory (DEM; Bussian, 1983). The electrical conductivity of the partially saturated soil matrix (σ_{sm}, S/m) is expressed as:

$$\sigma_{sm} = \phi_{sm}^{m_{sm}} \sigma_{f_{sm}} \left(\frac{1 - \sigma_s/\sigma_{f_{sm}}}{1 - \sigma_s/\sigma_{sm}} \right)^{m_{sm}}, \tag{2}$$

where m_{sm} (–) is the cementation exponent of the soil matrix, $\sigma_{f_{sm}}$ (S/m) is the effective electrical conductivity of the fluid mixture in the soil matrix and σ_s is the surface conductivity.

The effective electrical conductivity of the matrix fluid mixture is given by (Archie, 1942):

$$\sigma_{f_{sm}} = \left(\frac{\theta_{sm}}{\phi_{sm}} \right)^{N_{sm}} \sigma_w, \tag{3}$$

where θ_{sm} ($cm^3\ cm^{-3}$) is the volumetric water content of the soil matrix, N_{sm} (–) is the saturation exponent that accounts for the water distribution of the soil matrix, and σ_w (S/m) is the electrical conductivity of the pore water. Similarly, the electrical conductivity of the macropores (when zero, partially or fully saturated, σ_{mac} (S/m) can be expressed as:

$$\sigma_{mac} = \left(\frac{\theta_{mac}}{w_{mac}} \right)^{N_{mac}} \sigma_w, \tag{4}$$

where θ_{mac} ($cm^3\ cm^{-3}$) is the water content filling the macropores and N_{mac} (–) is the saturation exponent describing the water phase in the macropores. Finally, the electrical conductivity of the soil is obtained by applying DEM theory once again to predict the combined effects of the electrical conductivity of the soil matrix (σ_{sm}, resulting from the homogenization in Equation 2) and the electrical conductivity of the macropores (σ_{mac}, Equation 4):

$$\sigma_{soil} = (1 - w_{mac})^{M_{soil}} \sigma_{sm} \left(\frac{1 - \sigma_{mac}/\sigma_{sm}}{1 - \sigma_{mac}/\sigma_{soil}} \right)^{M_{soil}}, \tag{5}$$

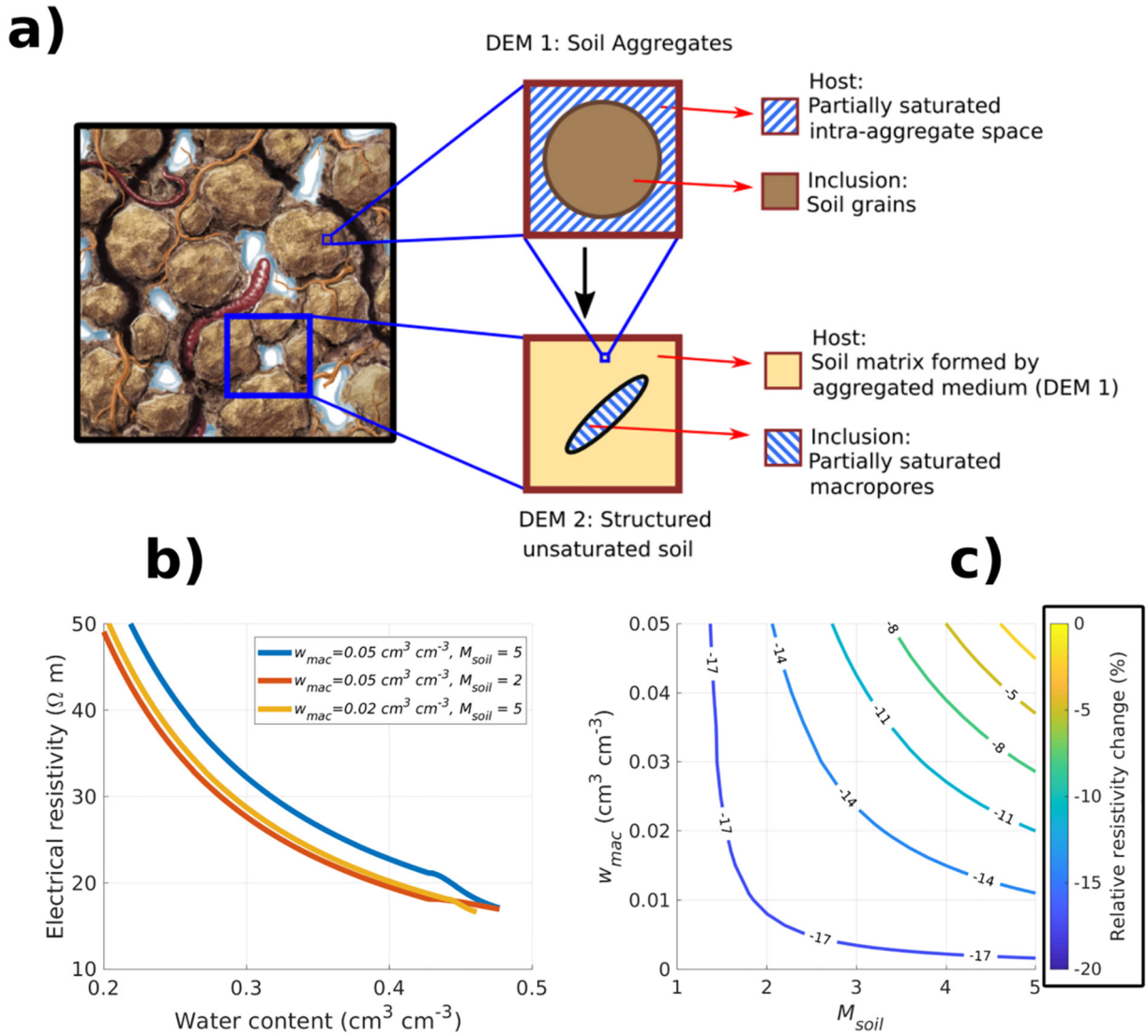

Figure 1. (a) Illustration of the pedophysical model used to link soil structure features with electrical conductivities of structured soils. The electrical conductivity of the soil aggregates is modeled by considering a hierarchy of fluid mixture with inclusions of soil grains and assembling a simple aggregated porous medium. The electrical conductivity of the structured soil is modeled by considering the soil as a porous matrix (represented as an assembly of aggregates) with inclusions representing soil macropores. The electrical conductivity of the partially saturated interaggregate space and macropores are modeled using Archie's second law. (b) Comparison of electrical resistivity as a function of water content for three combinations of the M_{soil} exponent (M_{soil} = 5, 2, and 5) and macroporosity (w_{mac} = 0.05, 0.05, and 0.02 cm^3 cm^{-3}). The soil matrix porosity (ϕ_{sm} = 0.46 cm^3 cm^{-3}), matrix cementation exponent (m_{sm} = 2), saturation exponents ($N_{sm} = N_{mac}$ = 2), the water conductivity (σ_w = 0.03 S/m), and the surface conductivity (σ_s = 0.1 S/m) are the same for the three cases. (c) Relative change of electrical resistivity calculated at a water content of θ = 0.38 cm^3 cm^{-3} as a function of M_{soil} and w_{mac} with respect to the base case (M_{soil} = 5 and w_{mac} = 0.05 cm^3 cm^{-3}).

where M_{soil} (–) is an exponent that is inversely related to the connectivity between soil aggregates (and related to the connectivity of the soil macroporous region). The macropores (assumed to be small compared to the averaging volume) are thus embedded in a soil matrix with homogeneous properties defined by Equation 2 (see also Figure 1a). The symbol M_{soil} is capitalized here to differentiate it with the more traditional cementation exponent m_{sm} for which large data sets are available (see Bussian, 1983; Cosenza et al., 2009; Friedman, 2005; Lesmes & Friedman, 2005). Equation 5 implies that the presence of macroporosity (when unsaturated, which is the most common state) hinders electrical conduction in the structured soil by (1) decreasing the volumetric proportion of the electrically conductive soil matrix ($1 - w_{mac}$) and (2) by interrupting electrical pathways between soil aggregates (M_{soil}).

For consistency with the literature dealing with DC-resistivity data (Binley & Kemna, 2005), we report electrical resistivities of the soil (ρ_{soil}, Ωm):

$$\rho_{soil} = \frac{1}{\sigma_{soil}}. \tag{6}$$

The sensitivity to changes in w_{mac} and M_{soil} is now illustrated by predicting the electrical resistivity of a soil as a function of water content (Figure 1b) assuming three different combinations of M_{soil} and w_{mac}: a base case ($M_{soil} = 5$, $w_{mac} = 0.05$ cm^3 cm^{-3}), a reduction in M_{soil} ($M_{soil} = 2$, $w_{mac} = 0.05$ cm^3 cm^{-3}), and a reduction of macroporosity ($M_{soil} = 5$, $w_{mac} = 0.02$ cm^3 cm^{-3}). The remaining parameters are kept constant and chosen as typical values found in the literature: the soil matrix porosity ($\phi_{sm} = 0.46$ cm^3 cm^{-3}), aggregate cementation exponent ($m_{sm} = 2$), the saturation exponents ($N_{sm} = N_{mac} = 2$), the water conductivity ($\sigma_w = 0.03$ S/m), and the surface conductivity ($\sigma_s = 0.1$ S/m; Farahani et al., 2018; Friedman, 2005; Revil et al., 2017). At full water saturation, the electrical resistivity is similar for all cases. At a given water content, the electrical resistivity decreases when reducing M_{soil} or w_{mac} as expected in response to a compaction event. This behavior is in agreement with laboratory and field observations (Besson et al., 2013; Keller et al., 2017; Seladji et al., 2010). At high water saturation, macropore activation (saturation of macropores) occurs and we observe a drop in electrical resistivity. Figure 1c illustrates the relative impact of changes in M_{soil} and w_{mac} on electrical resistivity. The values are calculated at a water content close to field capacity in agricultural soils ($\theta \sim 0.38$ cm^3 cm^{-3}) using the base case ($M_{soil} = 5$, $w_{mac} = 0.05$ cm^3 cm^{-3}) as the reference. Somewhat counter-intuitively, a compaction-induced decrease of w_{mac} have its strongest impact on the predicted electrical resistivity when the macropores are dry or partially saturated. The effect is larger by having a decrease in M_{soil}. It is expected that both M_{soil} and w_{mac} are modified by soil compaction. For the example presented in Figure 1c, the combined effects of reductions in M_{soil} and w_{mac} lead to a decrease of electrical resistivity by up to 20%.

2.2. Hydrological Process Modeling in Structured Soils

Soil water flow and heat transfer are known to be influenced by soil structure properties. By including such considerations in our modeling framework, we explicitly account for soil structural changes that may impact soil water dynamics sensed by geoelectrical monitoring. Herein, soil water flow and heat transfer are performed using the 1D software Hydrus-1D (Simunek et al., 2013).

2.2.1. Water Flow Modeling

One-dimensional water flow in unsaturated media is governed by Richards' equation, written as (Richards, 1931):

$$\frac{\partial \theta}{\partial t} = \frac{\partial}{\partial z}\left[K_{soil}\left(\frac{\partial h}{\partial z} + 1\right)\right] - \Gamma, \tag{7}$$

where h (cm) is the water pressure head, θ (cm^3 cm^{-3}) is the volumetric water content, z (cm) is the spatial coordinate, Γ (cm^3 cm^{-3}/h) is the sink term, and K_{soil} (cm/h) is the unsaturated hydraulic conductivity. We impose atmospheric boundary conditions at the top of the soil profile, precipitation, and evapotranspiration (as described below) and a free drainage boundary condition at the bottom of the soil profile. To account for soil structure, macropore water flow was modeled using the approach by Durner (1994), which divides the porous medium into two overlapping domains representing (1) the pore system in the soil matrix and (2) the macropore system. In this parametrization, the water retention and the hydraulic conductivity function of the soil are expressed as a combination of the functions ascribed to the two considered domains:

$$S_e = \frac{\theta - \theta_r}{\phi_T - \theta_r} = w_{sm}[1 + (\alpha_{sm}h)^{n_{sm}}]^{1-\frac{1}{n_{sm}}} + w_{mac}[1 + (\alpha_{mac}h)^{n_{mac}}]^{1-\frac{1}{n_{mac}}}, \tag{8}$$

and

$$K_{soil} = r_k K_{sm} \frac{\left(w_{sm} S_{e_{sm}} + w_{mac} S_{e_{mac}}\right)^{0.5}}{\left(w_{sm}\alpha_{sm} + w_{mac}\alpha_{mac}\right)^2} \left(w_{sm}\alpha_{sm} \left[1 - \left(1 - S_{e_{sm}}^{\frac{n_{sm}}{n_{sm}-1}} \right)^{1-\frac{1}{n_{sm}}} \right] + w_{mac}\alpha_{mac} \left[1 - \left(1 - S_{e_{mac}}^{\frac{n_{mac}}{n_{mac}-1}} \right)^{1-\frac{1}{n_{mac}}} \right] \right)^2, \quad (9)$$

where S_e ($cm^3\ cm^{-3}$) is the effective saturation of the soil, θ_r ($cm^3\ cm^{-3}$) is the residual water content, n_i (–) is the van Genuchten exponent (which is related to soil texture), and α_i (cm^{-1}) is related to the inverse of the air-entry pressure. The saturated hydraulic conductivity of the soil $K_{sat} = r_k K_{sm}$ is defined as the product of the saturated hydraulic conductivity of the soil matrix K_{sm} (cm/h) and the ratio r_k ($= K_{sat}/K_{sm}$) which is a function of the soil macroporosity. The indices $i = sm$ and $i = mac$ represent the soil matrix and the macroporous region, respectively. Note that these are the same two regions that are considered in the pedophysical model of electrical properties (see Section 2.1). By considering Equations 5 and 9, it is seen that a reduction of soil macroporosity reduces the soil electrical resistivity and the saturated hydraulic conductivity.

The higher saturated hydraulic conductivity of structured soils is often attributed to macropore networks created by bioturbation (earthworms moving and decaying roots; Bonetti et al., 2021). Soil biological activity and related soil organic matter are related to the saturated hydraulic conductivity of soils (Araya & Ghezzehei, 2019) and decay exponentially with respect to soil depth (Hobley & Wilson, 2016; Kramer & Gleixner, 2008). Consequently, we approximate the saturated hydraulic conductivity of the soil K_{sat} (cm/h) with a function that decays exponentially with soil depth to the saturated hydraulic conductivity of the soil matrix K_{sm} as:

$$K_{sat}(z) = K_{sm} + a_{K_0} e^{-z/\lambda_K}, \quad (10)$$

where a_{K_0} (cm/h) is the increase in saturated hydraulic conductivity at the soil surface due to macroporosity and λ_K (cm) is the depth at which the macroporosity-induced increase has been reduced by a factor $1/e$.

2.2.2. Representing Soil Structure Effects on Surface Evaporation

We now consider soil structure-induced changes in soil evaporation properties in order to link them to our pedophysical predictions. The dynamics of soil surface evaporation is typically characterized by two stages with different evaporation rates (Or et al., 2013). During Stage-I evaporation, soil evaporation is supported by capillary flow from a soil depth that is mediated by soil properties, the evaporation rate is at its maximum (determined by atmospheric conditions) and remains relatively constant. At a certain water content, hydraulic continuity with the evaporating surface is interrupted and the process transitions to Stage-II evaporation dominated by vapor diffusion determined by the drying front depth (often at significantly lower rates relative to Stage-I). Under a wide range of conditions, evaporative losses are determined by the duration of Stage-I evaporation and the depth for capillary continuity (the so-called soil evaporation characteristic length) that supports it. The transition from Stage-I to Stage-II evaporation occurs at a critical water content (θ_{crit}, $cm^3\ cm^{-3}$) marking the interruption of capillary pathways. Similarly, there is an associated critical pressure head (h_{crit}, cm) that marks such interruption. Lehmann et al. (2008) proposed to use the water retention properties of soil to estimate the critical pressure head as:

$$h_{crit} = \frac{1}{\alpha_{sm}\left(\frac{n_{sm}-1}{n_{sm}}\right)^{2-\frac{1}{n_{sm}}}}. \quad (11)$$

Then, h_{crit} can be used to calculate the soil evaporation characteristic length (L_c, cm; Lehmann et al., 2008; Or & Lehmann, 2019) representing the limiting depth at which there is an interruption in soil capillary flow supporting Stage-I evaporation as:

$$L_c = \frac{h_{crit} - h_b}{1 + \frac{E_0}{4K_{sm}(h_{crit})}} = \frac{\frac{1}{n_{sm}\alpha_{sm}}\left(1 + \frac{n_{sm}}{n_{sm}-1}\right)^{\left(2-\frac{1}{n_{sm}}\right)}}{1 + \frac{E_0}{4K_{sm}(h_{crit})}}, \tag{12}$$

where E_0 (cm/h) is the potential evaporation rate, typically taken as the mean potential yearly evaporation (e.g., Lehmann et al., 2019). In this study, we consider the soil evaporation properties (L_C and h_{crit}) to be a function of the water retention and hydraulic properties of the soil matrix. We hypothesize that as these parameters depend on soil structure, soil compaction impacts soil evaporation. The compaction-induced increase in aggregate connectivity with an associated decrease in electrical resistivity could result in an increase in capillary flow paths resulting in enhanced evaporation. These parameters are then used to define soil structure-specific evapotranspiration functions for our water flow model.

The characteristic evaporation length (Equation 12) and the critical pressure head (Equation 11) are used in combination with soil potential evapotranspiration (ET_p, cm/h) to define treatment-specific (vegetated and bare soil, compacted and non-compacted) potential evaporative water losses. Similarly to conventional approaches for modeling root-water uptake (Simunek et al., 2013), we modeled the potential water losses as the product of: (1) a linear combination of a root density function that is depth-dependent ($RU(z)$ (–)) and a soil evaporation function based on the concept of the soil evaporative capacitor (Or & Lehmann, 2019) that draws water from different depths (SE(z) (–)); (2) a scaling function varying between zero and one that depends on the soil pressure head ($\beta(h)$ (–)); and (3) a surface potential evapotranspiration rate determined by meteorological conditions as:

$$\Gamma_{ET} = \beta(h)\left((1-\chi_{ev})\frac{RU(z)}{\int_0^Z RU(z)dz} + \chi_{ev}\frac{\mathrm{SE}(z)}{\int_0^Z SE(z)dz}\right)ET_p(t), \tag{13}$$

where Z (cm) is the depth of the soil profile and χ_{ev} (–) is the percentage of flux associated with soil evaporation. The potential evapotranspiration ET_p is calculated using the empirical function based on soil temperature by Jensen and Haise (1963). For simplicity, the depth-dependent evaporation function is defined as a normalized function of the soil characteristic evaporation depth. It is expressed as:

$$\mathrm{SE}(z) = \begin{cases} \frac{5}{3L_c} & z < 0.2L_c \\ \frac{2.083\,3}{L_c}\left(1 - \frac{L_c - z}{L_c}\right) & 0.2L_c < z < L_c \\ 0 & z > L_c. \end{cases} \tag{14}$$

The depth-dependent root distribution function is chosen as an exponential function decaying with depth (e.g., Zuo et al., 2006):

$$RU(z) = RU_0 e^{-z/\lambda_{roo}}, \tag{15}$$

where RU_0 (–) is the root density at the soil surface and λ_{roo} (cm) is the depth at which root density has decayed to $1/e$ of RU_0. We defined the scaling function $\beta(h)$ as a S-shape function:

$$\beta(h) = \frac{1}{1 + \left(\frac{h}{h_{50}}\right)^p}, \tag{16}$$

with the exponent p (–) determining how fast β drops with increasing pressure head and h_{50} (cm) is the pressure head at which β is equal to 0.5 (Feddes, 1978).

In the absence of vegetation, we have that $\chi_{ev} = 1$ (i.e., no root-water uptake) and the function $\beta(h)$ can be used to approximate the soil evaporation function representing the transition from Stage-I evaporation to Stage-II evaporation by approximating the h_{50} as the critical capillary pressure h_{crit}. Conversely, $1 - \chi_{ev}$ determines the fraction of water available for root-water uptake and evaporation in vegetated soils. This is similar to the time-dependent soil transpiration coefficient that accounts for limited evaporation due to soil cover (Hanks, 2012). In vegetated soils, $\beta(h)$ represents the so-called root-water stress function (see van Genuchten, 1987).

2.2.3. Heat-Transfer Modeling

In order to incorporate temperature effects on the monitored geoelectrical data, one-dimensional heat-transfer modeling is considered. Heat transfer is described by a convection-dispersion equation, defined for a one-dimensional system as:

$$C_p(\theta)\frac{\partial T}{\partial t} = \frac{\partial}{\partial z}\left[\lambda(\theta)\frac{\partial T}{\partial z}\right] - C_w q\frac{\partial T}{\partial z}, \tag{17}$$

where T (°C) is the temperature, $\lambda(\theta)$ ($Wm^{-1}\,°C^{-1}$) is the coefficient of the apparent thermal conductivity of the soil, which includes effects of heat transfer by vapor movement (Sophocleous, 1979), C_p ($Jm^{-3}\,°C^{-1}$) and C_w ($Jm^{-3}\,°C^{-1}$) are the volumetric heat capacity of the porous media and the water, respectively, and q is the Darcy fluid flux. The volumetric heat capacity of the soil can be expressed as (De Vries, 1963):

$$C_p(\theta) = (1-\phi_T)C_s + \theta C_w, \tag{18}$$

C_s ($Jm^{-3^o}C^{-1}$) and C_a ($Jm^{-3}\,°C^{-1}$) are the volumetric heat capacity of the soil solid phase and the air, respectively. We use air temperature at 5 cm height as the top boundary condition and a zero-gradient lower boundary condition.

2.3. Coupled Hydrogeophysical Modeling

A coupled hydrogeophysical modeling scheme is used to investigate the soil structure signatures on soil water dynamics (see Section 2.2) and their corresponding geoelectrical signatures (see Section 2.1). The modeling is divided in two main parts (see Figure 2) that are described below.

2.3.1. Part I: Forward Modeling of Water Flow and Heat Transfer

The hydraulic and transport properties of the soil matrix are used to compute the soil evaporative properties (Equations 11 and 12). Soil transport and hydraulic properties (soil matrix and macropores) and the evaporative properties are then used to model water flow in Hydrus-1D. From this, we obtain time series of soil evapotranspiration, water content, and temperature at specific depths and profiles of water content and temperature. For simplicity, the time series of water content at measurement depths are converted to relative permittivities by using the widely used volumetric mixing model known as the Complex Reflective Index Model (CRIM; Roth et al., 1990). The relative permittivity of the soil is expressed as:

$$\sqrt{\kappa_{soil}} = f_s\sqrt{\kappa_s} + f_w\sqrt{\kappa_w} + f_a\sqrt{\kappa_a} + f_{ice}\sqrt{\kappa_{ice}}, \tag{19}$$

where κ_{soil} (–), κ_s (–), κ_w (–), κ_a (–), κ_{ice} (–) are the relative permittivities of the soil, the soil grains, the soil water, the air, and the ice, respectively. Similarly, $f_s = 1-\phi_T$ ($cm^3\,cm^{-3}$), $f_w = \theta(1-S_{ice})$ ($cm^3\,cm^{-3}$), $f_a = \phi_T - \theta$ ($cm^3\,cm^{-3}$), and $f_{ice} = \theta S_{ice}$ ($cm^3\,cm^{-3}$) refer to the fraction of soil grains, water, air and ice, respectively. The ice saturation (S_{ice}) is approximated at a given time as a linear function of the mean soil temperature from the previous 24 hr at the evaluated soil depth. The onset for obtaining nonzero values in ice content was defined when the mean temperatures fell below 0.5 °C. In addition, we considered temperature effects on the relative permittivity of water κ_w using the widely applied model found in Weast et al. (1988).

2.3.2. Part II: Inverse Modeling of Soil Electrical Data

The simulated water content profiles are fed to the pedophysical model (Equations 2–6) to derive electrical resistivity profiles. Subsequently, the temperature profiles are used to calculate temperature-dependent profiles of electrical resistivity with the model by Campbell et al. (1948) with the standard choices of the corresponding parameters: $\alpha_{cam} = 0.0202$ and $\beta_{cam} = 0.517$. Finally, the apparent resistivities are simulated for a desired electrode array. We solve the 1D DC-resistivity problem (e.g., Parker, 1984) for a Wenner-Schlumberger array using an electrode spacing of $a = 50$ cm and various current-electrode spacings ($(2j+1)a$) corresponding to $j = 1, 2, 3,$ and 4. This is achieved using the numerical implementation by Ingeman-Nielsen and Baumgartner (2006) that is based on digital filter theory.

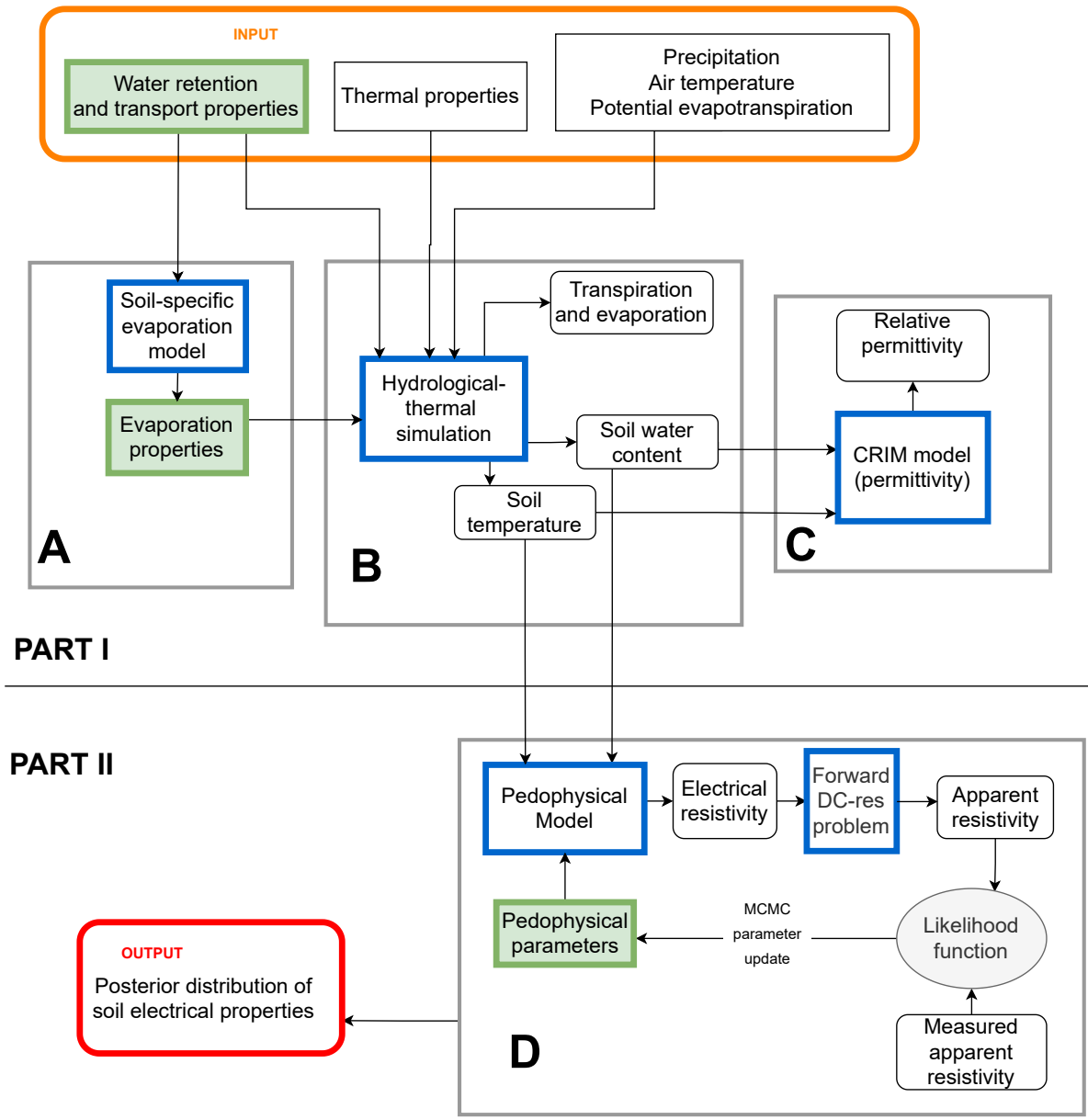

Figure 2. Flowchart describing our hydrogeophysical framework including forward hydrological modeling with soil evaporation constraints (Part I) and inverse modeling of geoelectrical data (Part II) where the properties influenced by soil structure are highlighted in green. The flowchart is divided in blocks containing different modeling steps involved in the coupled model. In A, water retention and transport properties are used to calculate treatment-specific evaporation properties. In B, the water retention, transport and evaporation properties are used to perform a hydrothermal simulation with Hydrus-1D resulting in soil water fluxes, water content and temperature. In C, the water content time series are used with the CRIM model for calculating the relative permittivities considering temperature effects for comparison with TDR data. The inverse modeling of the electrical data is represented in D The water content and temperature are used with the new pedophysical model to compute electrical resistivity profiles that are in turn used to compute apparent electrical resistivity. The posterior distributions of pedophysical electrical properties are inferred using MCMC.

The pedophysical electrical properties ($\mathbf{P} = [\sigma_{sm}, \sigma_w, m_{sm}, M_{soil}]$) are inferred using the Markov-chain Monte Carlo (MCMC) method by Laloy and Vrugt (2012) (the so-called differential evolution adaptive Metropolis, $\text{DREAM}_{(ZS)}$) to infer the posterior probability density function of the electrical properties using the following likelihood function

$$L(\mathbf{P}|\mathbf{d}) = \left(\sqrt{2\pi\sigma_{\mathbf{d}}}\right)^{-N} \exp\left[-\frac{1}{2}\sum_{i=1}^{N}\left(\frac{F_i(\mathbf{P};\theta,T) - d_i}{\sigma_{d_i}}\right)^2\right], \quad (20)$$

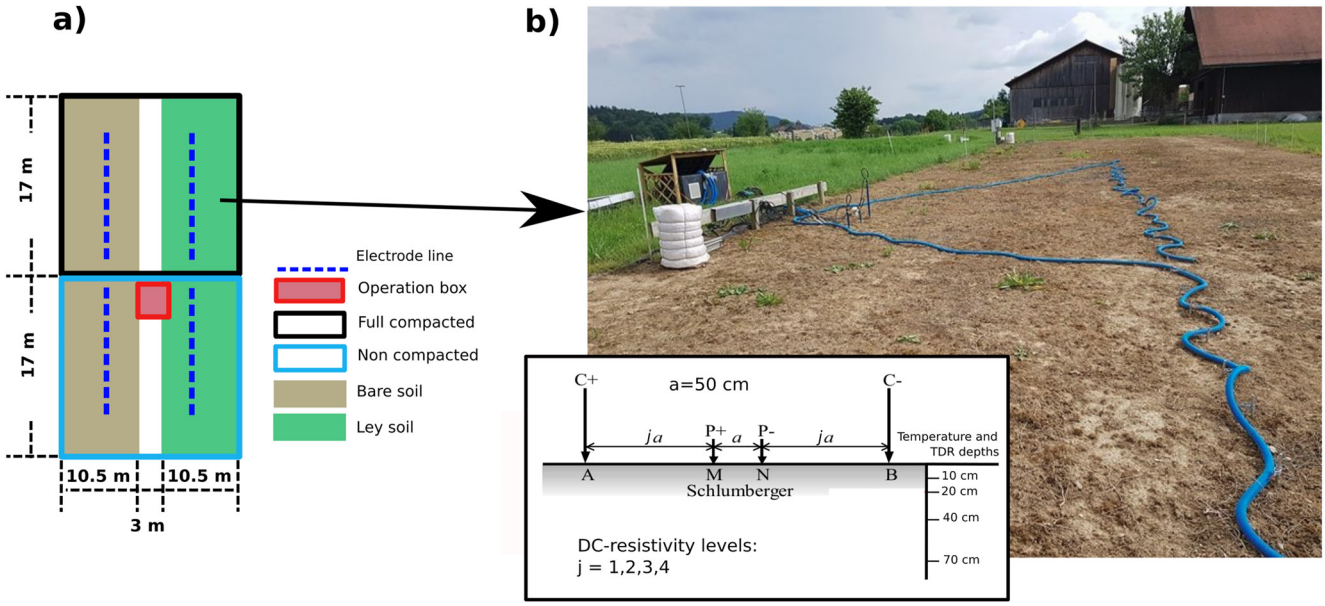

Figure 3. (a) Schematic representation of the DC-resistivity lines deployed in the SSO. (b) DC-resistivity line located in the bare soil.

where $F(\mathbf{P}; \theta, T)$ and $\mathbf{d}$ are the simulated and measured apparent resistivity, respectively, σ_{d_i} is the standard deviation of ith apparent resistivity datum and N is the number of data.

3. Data Monitoring at the SSO

To evaluate the value of electrical resistivity monitoring to capture long-term soil compaction and its effect on soil moisture dynamics, we conducted seasonal and bi-hourly geoelectrical monitoring. The monitoring was carried out at an experimental field site located in the vicinity of Zürich, Switzerland (8°31′04°E, 47°25′39°N; Keller et al., 2017). This SSO is a long-term experiment designed to study the evolution of soil structure, following a compaction event in the spring of 2014, for different types of postcompaction management (see Figure 3). We monitored the DC-resistivity response of experimental plots with two different covers (bare soil and ley soil) and two compaction treatments (compaction on the full surface and no compaction). The four experimental plots are referred to as full compacted ley (CL; grass-legume mixture), non-compacted ley (NL), full compacted bare soil (CB), and non-compacted bare soil (NB). The soil properties (and texture) prior to the compaction event were similar at all monitoring sites (Keller et al., 2017) allowing us to attribute differences in electrical signatures to different soil covers and treatments.

For the seasonal monitoring, the DC-resistivity acquisition array comprised two lines of 48 stainless steel electrodes: one line on the ley soil and the other on the bare soil. The electrode spacing was 1 m, resulting in 47.5 m long DC-resistivity lines. To enhance the spatial resolution, the electrode spacing was changed to 50 cm in the spring of 2015. With this change, 24 electrodes were placed on the compacted treatment and 24 on the non-compacted treatment for each electrode line in the ley and bare soil. The seasonal campaigns extend from March 2014 (a few weeks before the compaction event) until March 2021.

In this study, we focus primarily on interpreting geoelectrical data from bi-hourly monitoring. In this case, the electrodes were connected to a 96-switch Syscal-Pro powered by a 12 V battery located in an operation box at the edge of the experimental plots (see Figure 3). The Syscal-Pro was controlled by a laptop operating the Comsys-Pro geophysical software (see http://www.iris-instruments.com/download) continuously. A DC-resistivity acquisition sequence was programmed to be repeated every 2 hr. Data were first collected from the bare soil profile and then from the ley soil profile. The same subsequence (considering only 48 electrodes) was applied to both lines. A full DC-resistivity acquisition consisted of 464 data points (no stacking) for each profile, the duration of the current injection cycle was set to 250 ms and the full acquisition was completed in one and a half hours. We used a Wenner-Schlumberger electrode array with 50 cm spacing between potential electrodes and

four different spacings ($(2j + 1)a$) for current electrodes corresponding to $j = 1$, 2, 3, and 4 (see Figure 3b). The different lateral values of apparent resistivity were averaged to obtain one value for each level at each plot at a given acquisition time. Thus, the soil structure (compaction) treatments are assumed to be laterally homogeneous and we focused on larger-scale differences at the plot scale. Data were collected from February 15 to July 8. Due to technical issues with the monitoring system, apparent electrical resistivity data were not available during three periods of the monitoring campaign. In addition, we note that the sequences for seasonal and bihourly monitored geoelectrical data (including both arrays with 0.5 and 1 m spacings) contain data from a Wenner array with 1 m electrode spacing.

To supplement geoelectrical measurements and link to hydrological dynamics, we monitored water content with time-domain reflectometry (TDR). Soil temperature was monitored to correct the temperature-dependent geoelectrical data. TDR (TDR 100 by Campbell Scientific with MDX multiplexers) and temperature probes were installed in all experimental plots, and were continuously collecting data every hour at four different depths (10, 20, 40, and 70 cm, Figure 3b). Meteorological data were continuously monitored at an on-site station.

Aboveground biomass was measured in the ley treatments from three replicates of the experiment shown in Figure 3a (see more experimental details in Keller et al., 2017). These data were collected to evaluate soil compaction effects on plant growth. Measurements were made in the Spring of 2017 only.

4. Model Application: Soil Compaction and Surface Cover Treatments

Our main objective is to interpret geoelectrical data in terms of soil structure and its associated influence on soil transport and evaporation properties. In this section, we (1) highlight the main soil structure-related features observed in the monitored geoelectrical and hydrological data, (2) explain our strategy for integrative modeling aiming at capturing such features, and (3) present details concerning the MCMC inverse modeling for inferring electrical properties of compacted and non-compacted soils.

4.1. Insights Concerning Soil Structure Impacts on Water Dynamics and Geoelectrical Data

Figure 4a presents the averaged apparent resistivity time series ($j = 1$ of Wenner-Schlumberger array) for all four experimental plots. The averaged standard deviations for this monitoring period were 3.86, 4.33, 2.21, and 2.23 Ωm for compacted ley, non-compacted ley, compacted bare and non-compacted bare soil, respectively (see Romero-Ruiz, 2021, for all standard deviations). This level of the Wenner-Schlumberger array is sensitive to shallow soil water dynamics and, thus, is expected to contain the strongest imprint related to soil structure and compaction. Figure 4b presents the soil water storage of the upper one m of the soil estimated from TDR data. We present soil water storage to show an integrated quantity (i.e., considering variations at all measured depths) of soil water dynamics.

Three main features are observed in Figure 4: (1) compacted soils become drier than non-compacted soils in dry months—this effect is captured by both geoelectrical data and water dynamics; (2) soil compaction produces a decrease in apparent resistivity, particularly during wet months—this is observed in the geoelectrical data and complemented by the presented water storage; and (3) there is a strong seasonal influence of soil temperature in the geoelectrical data—this effect is present in all experimental plots and is not associated to soil compaction. Clearly, soil water dynamics and temperature exert a strong influence on the monitored geoelectrical data. During wet periods outside of the growing season (i.e., high values of water storage for all experimental plots before March 31), the apparent resistivities cluster according to the compaction treatment with higher values for non-compacted ley and bare soil than for compacted ley and bare soil. Under these conditions (see data before March 31 in Figure 4a), soil compaction has resulted in a decrease in soil electrical resistivity (∼15%). This effect persists during the full monitoring period in the bare soil with the values of compacted bare soil consistently shifted to lower values compared with non-compacted bare soils. The apparent electrical resistivity of the bare soil follows a mainly temperature-driven seasonal trend. The apparent resistivity of ley soil strongly responds to water storage variations during the growing season in May, June, and July 2018 (Figure 4a). Since compacted ley is typically drier in these months (see Figure 4b), the apparent resistivities of compacted ley reach similar values as non-compacted ley. This indicates that the impact of water content mask the impact of soil compaction in geoelectrical data. Figure 4c shows a crossplot of apparent resistivities and water storages monitored after May 9, 2018. Given that the water content effect is much stronger than the temperature induced seasonal trend in the

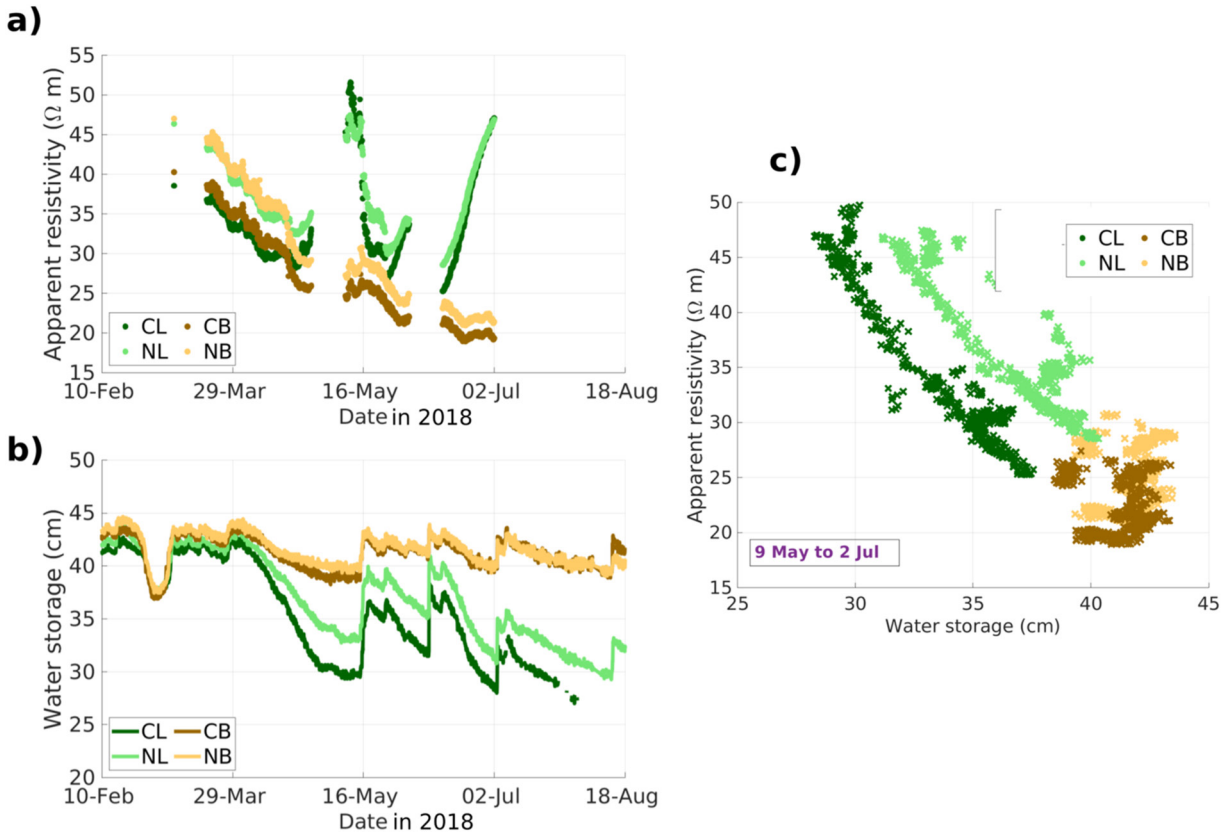

Figure 4. (a) Apparent electrical resistivity time series collected for compacted ley (CL), non-compacted ley (NL), compacted bare soil (CB), and non-compacted bare soil (NB), corresponding to $j = 1$ of the Wenner-Schlumberger array. (b) Soil water storage in the upper 1 m of the soil calculated from TDR data for all experimental plots presented in this study. (c) Crossplot of apparent resistivity adn water storage measured from 9 May to 2 July.

ley soil, we observe a clear drop in apparent resistivity for compacted soils for the same water storage (similarly to the predictions by our model shown in Figure 1b). Apparent resistivities from the bare soil remain dominated by the temperature trend.

In addition, we considered aboveground biomass measured at the SSO. The measured aboveground biomass averaged for all blocks in compacted ley (85 g/0.25 m^2) was approximately 70% of the biomass measured in the non-compacted ley (125 g/0.25 m^2). This suggests that plant transpiration in the compacted ley is lower in than in the non-compacted ley (see e.g., Steduto et al., 2007).

4.2. Part I: Modeling of Hydrological Data

The soil water retention and hydraulic properties for the different soil experimental plots were chosen based on hydrological observations in Section 4.1 (e.g., compacted soils have lower water storages during the growing season) and our knowledge of soil hydraulic properties for compacted and non-compacted soils at the SSO informed by the laboratory measurements by Keller et al. (2017). We consider a simplified conceptual model capturing salient features associated with soil structure that are considered important for soil hydrological regimes (drainage dynamics and surface evaporation) and their geoelectrical signatures. Consequently, we opted for a simple parametrization to differentiate between soil structure effects of compacted and non-compacted only in terms of: (1) the saturated hydraulic conductivity as a function of soil depth that accounts for macroporosity reduction, (2) the macroporosity as a function of soil depth, and (3) the van Genuchten parameter α_{sm} that accounts for aggregate connectivity. The remaining model parameters are considered constant with depth and the same for compacted and non-compacted soils. The choices of soil model parameters are summarized in Table 1 and detailed below. A detailed consideration of the complex spatial heterogeneity of soils is beyond the scope of our work.

Table 1
Soil Water Retention, Transport, Evaporation, Dielectric, Electrical, and Other Hydrus-1D Properties Considered in This Study for Non-Compacted Ley (NL), Compacted Ley (CL), Non-Compacted Bare Soil (NB), and Compacted Bare Soil (CB)

	NL	NB	CL	CB	Equation	Comments
Water Retention, Transport, and Evaporation Properties						
θ_r ($cm^3\ cm^{-3}$)	0.08	0.08	0.08	0.08	8	From Carsel and Parrish (1988)
ϕ_{sm} ($cm^3\ cm^{-3}$)	0.47	0.47	0.45	0.45	2 and 3	From Carsel and Parrish (1988)
ϕ_T ($cm^3\ cm^{-3}$)		$(1-w_{mac})\phi_{sm}+w_{mac}$			8	Computed
a_{K_0} (cm/h)	41.2	41.2	4.4	4.4	10	Assumed property
α_{sm} (cm^{-1})	0.04	0.04	0.02	0.02	8, 9, 11, and 12	Assumed property
n_{sm} (–)	1.15	1.15	1.15	1.15	8, 9, 11, and 12	Assumed property
K_{sm} (cm/h)	7.3	7.3	7.3	7.3	9, 10, and 12	Based on lab data
α_{mac} (cm^{-1})	1	1	1	1	8 and 9	Assumed property
n_{mac} (–)	2	2	2	2	8 and 9	Assumed property
h_{crit} (cm)	250	250	500	500	11 and 12	Computed
θ_{crit} ($cm^3\ cm^{-3}$)	0.35	0.35	0.33	0.33	–	Computed
L_c (cm)	31	31	63	63	12	Computed
Other Hydrus-1D Properties						
λ_{roo} (cm)	20	20	20	20	15	Assumed property
λ_K (cm)	18	18	18	18	10	Assumed property
p (–)	2	2	2	2	16	Assumed property
h_{50} (cm)	10^5	10^5	h_{crit}	h_{crit}	16	Approximated
C_s ($10^6\ Jm^{-3}\ °C^{-1}$)	1.92	1.92	1.92	1.92	18	From De Vries (1963)
C_w ($10^6\ Jm^{-3}\ °C^{-1}$)	4.18	4.18	4.18	4.18	18	From De Vries (1963)
Dielectric Properties						
κ_s (–)	5	5	5	5	19	From Annan (2005)
κ_w (–)	80	80	80	80	19	From Annan (2005)
κ_a (–)	1	1	1	1	19	From Annan (2005)
κ_{ice} (–)	3.4	3.4	3.4	3.4	19	From Evans (1965)
Electrical Properties						
M_{soil} (–)	x_1	x_1	x_2	x_2	5	Inverted properties [1, 5]
σ_s (S/m)	x_3	x_3	x_3	x_3	2	Inverted property [0, 0.25]
σ_w (S/m)	x_4	x_4	x_4	x_4	3 and 4	Inverted property [0.02, 0.05]
m_{sm} (–)	x_5	x_5	x_5	x_5	2	Inverted property [1.5, 2.5]
N_{sm} (–)	2	2	2	2	3	Assumed property
N_{mac} (–)	2	2	2	2	4	Assumed property

Note. The properties showing a value are fixed during the inversion whereas the properties showing an x_i are considered unknown. Some properties are common and some are different for each soil structure for both variable and fixed properties. The corresponding equation numbers are indicated.

4.2.1. Soil Macroporosity

Modeling the saturated hydraulic conductivity (K_{sat}) with the model by Durner (1994) (Equation 9) allows us to assume that the saturated hydraulic conductivity of the soil matrix K_{sm} has not been modified by compaction as suggested by Berli et al. (2006). Therefore, the saturated hydraulic conductivity $K_{sat}(z)$ of both compacted and non-compacted soils is modeled by Equation 10 with a common K_{sm} that is assumed constant with soil depth. The parameters of Equation 10 were obtained by fitting laboratory data of saturated conductivity of compacted and non-compacted soil at the SSO (Keller et al., 2017; see Figure 5a). We obtained $K_{sm} = 7.3$ cm/hr and $\lambda_K = 18$ cm

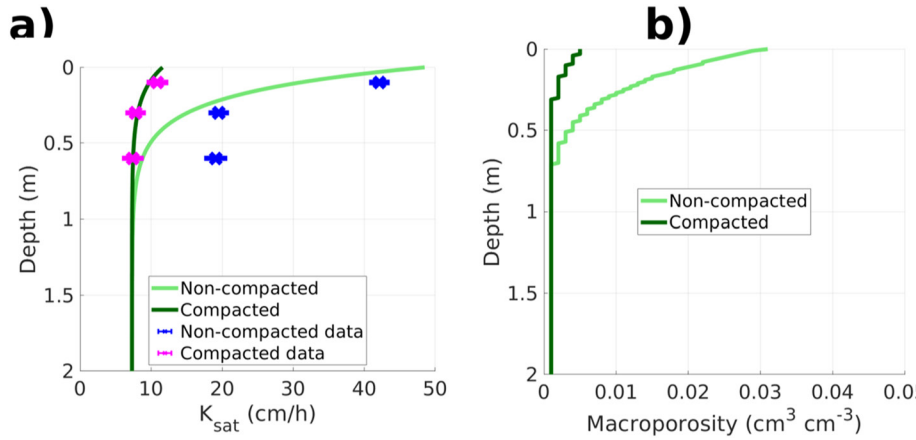

Figure 5. (a) Measured and predicted saturated hydraulic conductivity as a function of soil depth for compacted and non-compacted soils at the SSO. (b) Estimated macroporosity as a function of soil depth for compacted and non-compacted soils at the SSO.

for both compacted and non-compacted soils; and $a_{K_0} = 4.4$ and 41.2 cm/hr for compacted and non-compacted soils, respectively.

The variation of macroporosity with soil depth is obtained from the derived K_{sat} (z; Figure 5a). To link K_{sat} with soil macroporosity, we approximate the hydraulic conductivity function used here (Equation 9) by a linear superposition weighted by their volumetric fractions (see e.g., Fatichi et al., 2020) of (1) the hydraulic conductivity function of the soil matrix $K_{matrix}(h, z)$ and (2) the hydraulic conductivity function of the macropore system $K_{macropore}(h, z)$ as:

$$K_{soil} = w_{sm} K_{matrix}(h, z) + w_{mac} K_{macropore}(h, z). \tag{21}$$

With these assumptions, we infer a macroporosity at the soil surface of 0.5% and 3.1% for compacted and non-compacted soils, respectively (see Figure 5b).

4.2.2. Consideration of Changes in Soil Aggregate Contacts

In our model, soil evaporation properties strongly depend on three main properties: (1) the van Genuchten exponent n_{sm}, (2) the inverse of the air-entry pressure α_{sm}, and (3) the hydraulic conductivity of the soil matrix K_{sm}. The exponent n_{sm} is often regarded as a surrogate variable for soil texture which is roughly the same for the soil treatments studied here (25% clay, 25% sand, and 50% silt; see Keller et al., 2017) and is, consequently, considered the same for all experimental plots. We account for subtle soil compaction impacts on the soil matrix (increase in aggregate connectivity) using the parameter α_{sm} and assign the same α_{sm} for a given compaction treatment regardless of soil cover. This differentiation is motivated by the existence of subtle changes in mesoporosity (pore diameters in the range of 30–100 μm) between compacted and non-compacted soils as supported by observations and modeling by Meurer et al. (2020) who found differences in mesoporosity of compacted and non-compacted soils at the SSO. Here, we do not explicitly account for three domains (micropores, mesopores, and macropores) as done by Meurer et al. (2020). To simplify the analysis, we account for mesoporosity reduction as a reduction of α_{sm} for compacted soils and incorporate its corresponding effects on evaporation properties (Equations 11 and 12). This effect is implicitly accounted in the pedophysical model by considering both reduction in macroporosity and increase in aggregate connectivity. The parameter α_{sm} should decrease with compaction due to the closure of mesopores in the matrix induced by the applied stresses during compaction. The selected properties were $\alpha_{sm} = 0.04$ cm^{-1} for non-compacted soils, $\alpha_{sm} = 0.02$ cm^{-1} for compacted soils. Despite presenting a lower α_{sm}, studies suggest that hydraulic conductivity of compacted soil might be higher than for non-compacted soils under partially saturated conditions (see Aravena et al., 2014). For this reason, selecting a common K_{sm} for compacted and non-compacted soils despite the differences in α_{sm} remains a sensible choice. The exponent was set $n_{sm} = 1.15$ for all experimental plots. The selected values are within the range of properties for loamy-clay soils reported by Carsel and Parrish (1988).

The resulting evaporation properties obtained using Equations 11 and 12 are L_C = 31 cm and h_{crit} = 250 cm for non-compacted soils, and L_C = 63 cm and h_{crit} = 500 cm for compacted soils. The macroporosity, the total porosity (Equation 1) and saturated hydraulic conductivity of the soil vary with the soil depth. We selected α_{mac} = 1 cm^{-1} and n_{mac} = 2, leading to a pore size distribution of the soil macroporosity with a maximum pore radius of 1.5 mm. Water flow and heat-transfer simulations were made in a 3.5 m deep soil profile from August 6, 2017 to 18 August 2018. We discretized the soil in 20 different soil layers. Based on the observed difference on water storage between ley soil and bare soil, we assumed that the growing season (i.e., period in which both evaporation and transpiration are active in the ley soil) begins in the second week of April and ends in the third week of September.

4.2.3. Soil Dielectric and Thermal Properties

The dielectric properties of the soil are considered the same for all experimental plots. The dielectric properties of soil solid constituents, water, air, and ice were taken from the literature (Annan, 2005; Evans, 1965). Similarly, the values of the volumetric heat capacity of water and soil solids were chosen as typical values reported in the literature (De Vries, 1963). These values are reported in Table 1.

4.3. Part II: MCMC Inversion of Electrical Properties

For simplicity, all electrical properties were considered constant with soil depth. In the inversion, data from all plots were considered together in a common data vector **d**. We inverted the pedophysical electrical properties including the M exponent for compacted (M_{soil_C}) and non-compacted soils (M_{soil_N}), the surface conductivity (σ_s), the water conductivity (σ_w), and the cementation exponent of the soil matrix (m_{sm}; see also Table 1). As explained in Section 4.2, the macroporosity was obtained from the saturated hydraulic conductivity (Figure 5) and kept constant. Thus, the exponent M_{soil} that is inversely related to the connectivity among soil aggregates was set to be the distinctive property for the compaction state of the soils. This implies also that any misspecification of macroporosity will show up in the inferred M_{soil} (see also Figure 1). The surface conductivity (σ_s), the water conductivity (σ_w), the cementation exponent of the soil matrix (m_{sm}) were set to be same for all experimental plots. The saturation exponents ($N_{sm} = N_{mac} = 2$) appearing in Equations 3 and 4 were considered the same for all experimental plots and were not inferred by inversion. The ranges of the uniform prior probability density functions of the inversion parameters are provided in Table 1. To account for inadequacies in the hydrological modeling and the underlying parameters, the data error was selected as 10% of each data point.

This procedure of pedophysical inference based on modeled water contents and temperatures is referred to as the *modeling-based* approach. In the Section S1 in Supporting Information S1, we present an alternative *interpolation-based* approach that relies on linear interpolation of measured water contents and temperature for obtaining the corresponding profiles. The inversion procedure for calibrating electrical properties is the same for the two approaches.

5. Results

5.1. Soil Moisture Dynamics

5.1.1. Relative Permittivity

In agreement with TDR observations, the simulated relative permittivities do not show major differences between compacted and non-compacted bare soil at 10 cm depth (Figure 6a). Similarly, the observed slight differences between compacted and non-compacted soil at 40 cm depth are qualitatively captured by the simulations (Figure 6b). The measured differences during wet periods can be attributed to slight differences in total porosity between the two compaction treatments. The differences in the dry periods are primarily caused by differences in evaporation properties. The lower values of relative permittivities are linked with the critical water content at which Stage-I evaporation is interrupted. The computed critical water contents (related to h_{crit}) are θ_{crit} = 0.35 cm^3 cm^{-3} for non-compacted and θ_{crit} = 0.33 cm^3 cm^{-3} for compacted bare soil. The simulated relative permittivities persistently underestimates the magnitude of the measured relative permittivities at 40 cm depth (see Figure 6b). Our strategy to estimate the relative permittivities of soils with partially frozen water volumes reproduced well the freezing-thawing event (sharp drop in κ_{soil} in late February, Figures 6a and 7a).

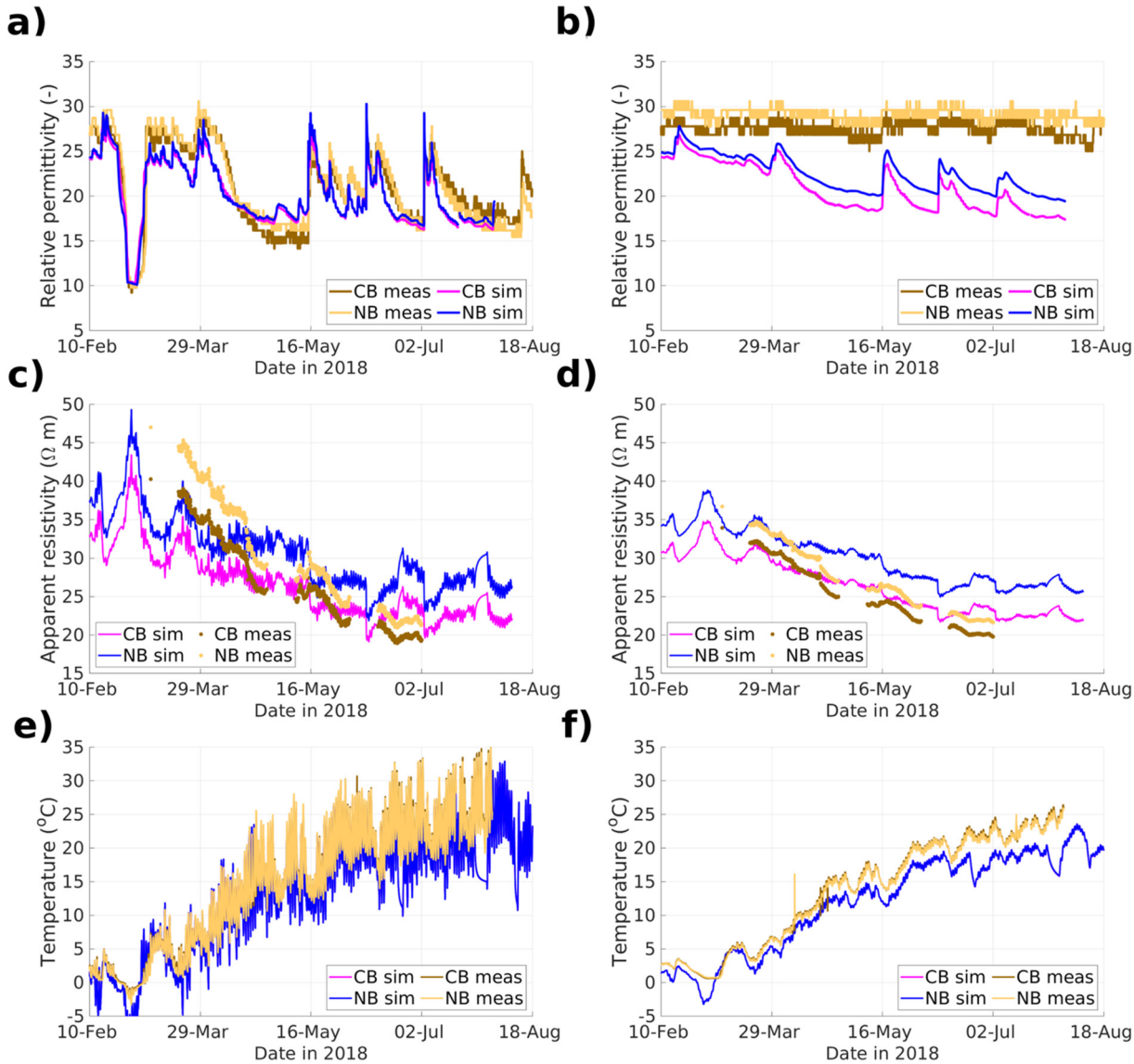

Figure 6. Simulated (sim) and measured (meas) relative permittivity of compacted and non-compacted bare soil at (a) 10 cm and (b) 40 cm depth. Simulated and measured apparent resistivity of compacted bare soil (CB) and non-compacted bare soil (NB) using (c) j= 1 and (d) j = 3 in the Wenner-Schlumberger array. Simulated and measured temperature of compacted and non-compacted bare soils at (e) 10 cm and (f) 40 cm depth.

In ley, the simulations are consistent with the observations at 10 and 40 cm depth (Figures 7a and 7b). We did not identify strong differences in relative permittivities of compacted and non-compacted soils at 10 cm depth (Figure 7a). The simulated relative permittivities captured the observed differences between compacted and non-compacted ley observed strong differences during dry periods at 40 cm depth (Figure 7b). Differences during wet periods can be interpreted as slight differences in total porosity between the two compaction treatments while differences during dry periods are associated with the combined effect of evaporation and root-water uptake. At 10 cm depth, the differences between treatments in the simulated relative permittivities are small, and in agreement with the measured data (Figure 7a). At this depth, the lowest values of the relative permittivities are limited by the pressure head at which the root-water uptake rate is reduced by half (h_{50}), which is the same for compacted and non-compacted ley. At 40 cm depth (Figure 7b), the differences between compacted and non-compacted ley are more visible. They are driven by differences in the characteristic evaporation length (L_c) that controls surface evaporation (Equation 14). At this depth, the simulated differences underestimate those observed by the TDR data.

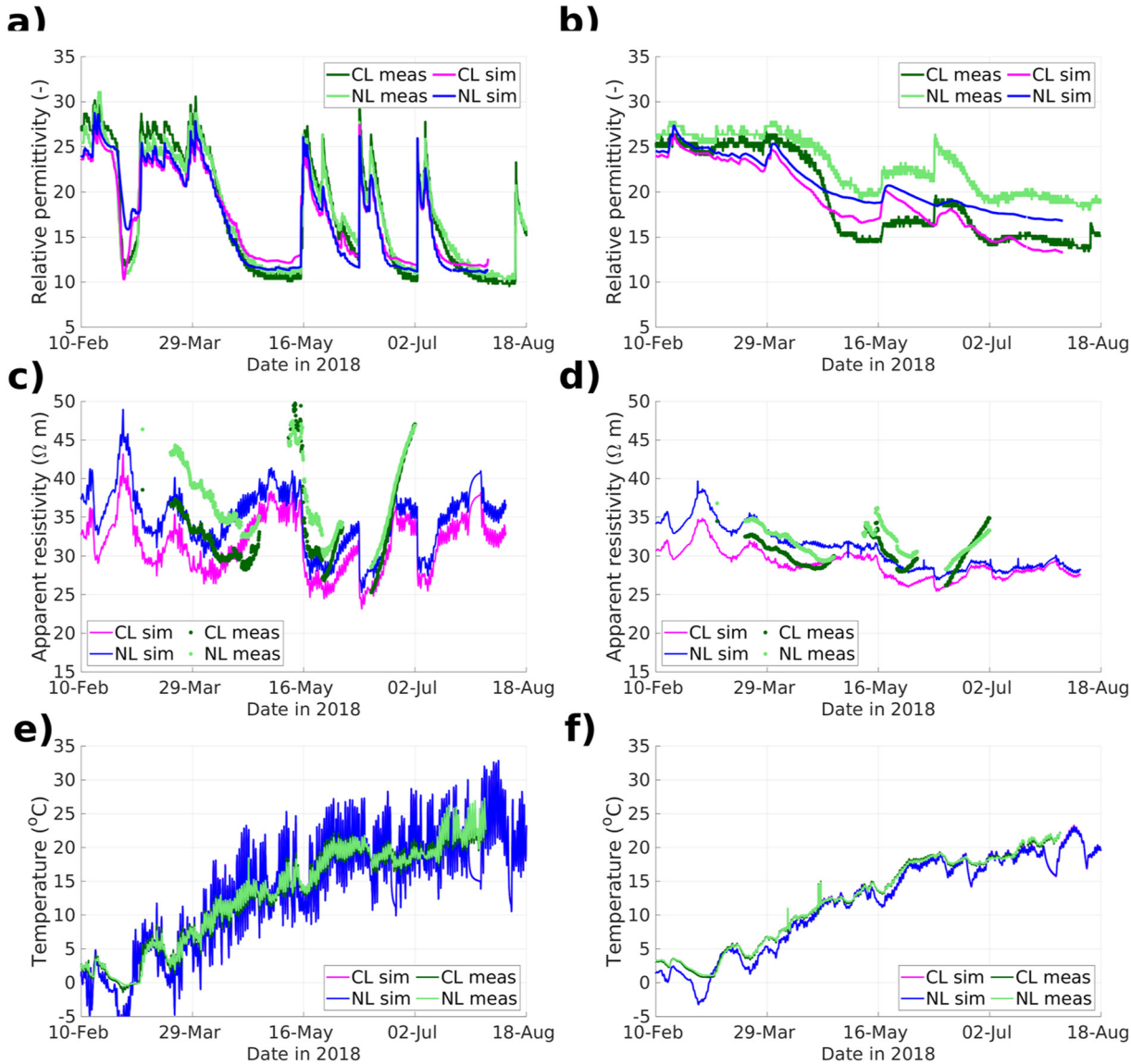

Figure 7. Simulated (sim) and measured (meas) relative permittivity of compacted and non-compacted ley soils at (a) 10 cm and (b) 40 cm depth. Simulated and measured apparent resistivity of compacted ley (CL) and non-compacted ley (NL) using (c) $j = 1$ and (d) $j = 3$ in the Wenner-Schlumberger array. Simulated and measured temperature of compacted and non-compacted ley soils at (e) 10 cm and (f) 40 cm depth.

5.1.2. Water Fluxes in Compacted and Non-Compacted Soils

We estimated water losses from water storage in the upper meter (adding the difference in water storage calculated for consecutive rain events) and compare them with the simulated water losses resulting from Hydrus-1D simulations (Figure 8) for which drainage occurs at the bottom of the soil profile. The measured annual water losses in the bare soil are approximately 61.8 and 59.6 cm for compacted and non-compacted bare soil, for which no root-water uptake or plant transpiration is considered in the modeling. This compares favorably with the simulated annual evaporation of 65.5 and 56.1 cm for compacted and non-compacted bare soil, respectively. The measured annual water losses were 110.1 and 95.4 cm for compacted and non-compacted ley, respectively. The simulated annual water losses were 107.3 and 103.6 cm for compacted and non-compacted ley, respectively. The model predicts an annual increase of 16.5 cm in evaporation for compacted ley relative to non-compacted ley.

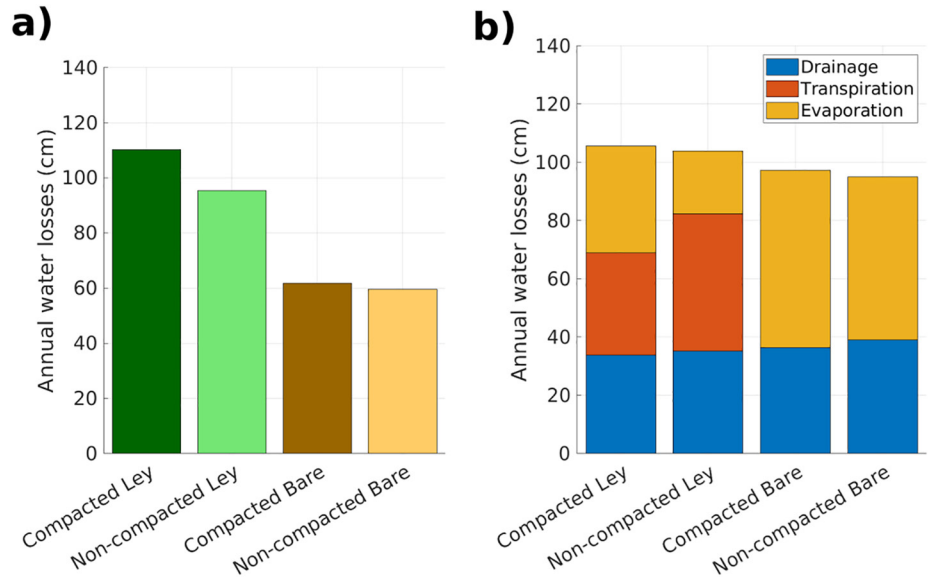

Figure 8. (a) Total annual water losses in the top meter of soils estimated from TDR data. (b) Total annual water losses in the top meter of soils resulting from the Hydrus-1D simulations. The different soil fluxes are marked with different colors for each soil treatment (compaction + cover) of the SSO.

5.2. Geoelectrical Data

5.2.1. Inverted Electrical Properties

Convergence of the MCMC chains was monitored using the $\hat{R}$-diagnostic by Gelman and Rubin (1992) using the common practice of declaring convergence when it is below 1.2 for all variables. Figures 9a, 9d, 9e and 9f present the corresponding posterior samples after burn-in (the first 1,000 iterations) for chains containing 8,000 iterations. Figures 9b and 9c show the difference and the crossplot, respectively, of the posterior estimates for exponents M_{soil} of compacted and non-compacted soils. The exponent M_{soil} presents mostly lower values for compacted soils (Figure 9b) compared to the non-compacted soils. This indicates that soil aggregates of compacted soils are more connected (i.e., the macroporosity is less connected) than for non-compacted soils. These results are supported by the results obtained using the *interpolation-based* approach presented in the Section S1 in Supporting Information S1. The reduction of M_{soil} together with the prescribed decrease in macroporosity explain the observed lower values of electrical resistivity of compacted soils even for similar values of water storage (see apparent resistivity and water storage in Figure 4). The sampled values of water conductivity and surface conductivity fall within reasonable ranges with respect to Farahani et al. (2018) and Revil et al. (2017), respectively (see also Section S1 in Supporting Information S1). The posterior mean of the cementation exponent of the soil matrix is 1.75.

5.2.2. Bihourly Apparent Electrical Resistivity

When using the modeling-based approach, the predicted apparent resistivities are adversely impacted by the discrepancies between the modeled and observed soil moisture dynamics discussed above. Yet, the main features observed in the measured apparent electrical resistivity are qualitatively well reproduced. The weighted root-mean-square-error (WRMSE, dimensionless) values (considering 10% data error) between measured and simulated apparent resistivities were 1.26, 1.05, 1.33, and 1.16 for compacted ley, non-compacted ley, compacted bare soil and non-compacted bare soil, respectively. Figures 6c and 6d present measured and simulated apparent resistivities for non-compacted and compacted bare soil for $j = 1$ and $j = 3$, respectively. The shift toward lower apparent resistivities for compacted soils is qualitatively well reproduced. There are two primary competing factors influencing the dynamics of soil apparent resistivity: soil temperature and soil water storage. For low temperatures and high water storage in the winter period, temperature effects dominate the apparent electrical resistivity. Conversely, for low water storage and high temperatures in the summer period, soil water storage dominates the electrical resistivity. Since the soil water storage varies within moderate to high values in the bare soil during

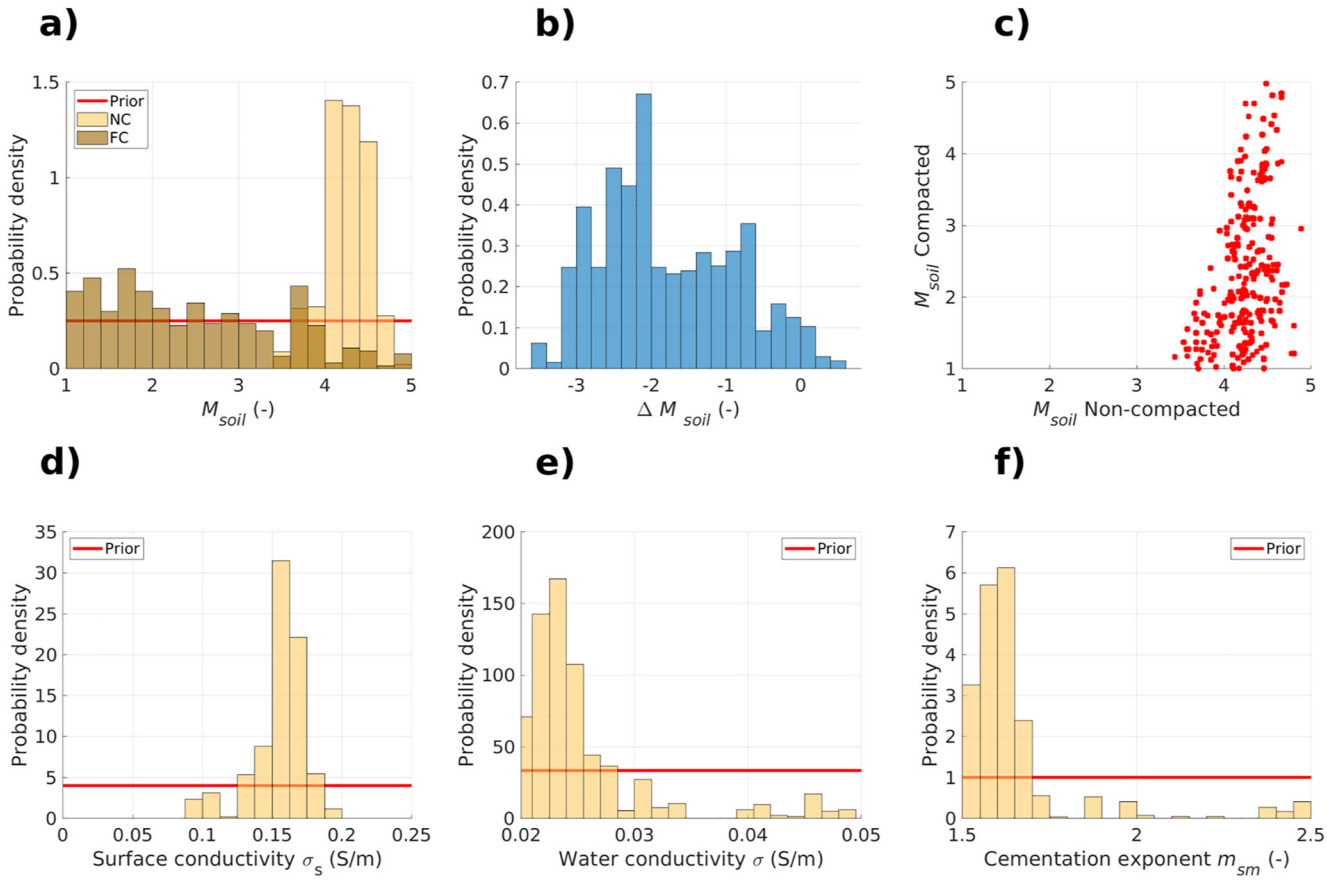

Figure 9. Results from MCMC inversion of geoelectrical data using the modeling-based approach after burn-in and for 8,000 iterations. Posterior MCMC estimate of (a) the exponent M_{soil} for non-compacted and compacted soil. (b) Difference between sampled values of M_{soil} for non-compacted and compacted soils. (c) Crossplot of the sampled values of M_{soil} for non-compacted and compacted soils. Posterior MCMC estimate of (d) surface conductivity (σ_s), (e) water conductivity (σ_w), and (f) the cementation exponent (m_{sm}). The latter three properties are shared for non-compacted and compacted soils.

the monitored period (see Figure 4a), the corresponding measured apparent resistivity is mainly responsive to the temperature-driven trends (see also Figures 6e and 6f). The simulations overestimated the measured apparent resistivity in the bare soil in early July as soil water losses are overestimated during this period (see Figure 6b). Note that the freezing event in 2018 occurred outside the period for geoelectrical monitoring and it is not expected to have an effect on the monitored data.

Figures 7c and 7d present measured and simulated data of apparent resistivity for non-compacted and compacted ley soil for $j = 1$ and $j = 3$, respectively. The measured apparent resistivity in the ley soil is strongly influenced by changes in soil water storage in the beginning of May and in the beginning of July (see also Figures 7a and 7b). These drying events are qualitatively well captured in the simulated apparent resistivities. The measured apparent resistivities in the compacted ley are initially lower than in non-compacted ley under wet conditions before switching to being higher under dry conditions (Figures 7c and 7d). This suggests that the compacted ley presents higher water losses during these dry periods. This effect is less evident in the simulated apparent resistivities, as the simulated differences in water losses and water content between compacted and non-compacted ley are underestimated. This feature is better reproduced using the interpolation-based approach presented in the Section S1 in Supporting Information S1.

5.2.3. Long-Term Seasonal Variations in Apparent Electrical Resistivity

Figure 10 presents the relative differences in apparent resistivity ($j = 1$, $a = 1$ m) considering compacted versus non-compacted bare soil and compacted versus non-compacted ley measured at the same date and time. We included data from the onset of the experimental compaction until March 2021 (~7 years after compaction). The simulations presented in Figure 10 were obtained using the electrical properties inferred for the bihourly

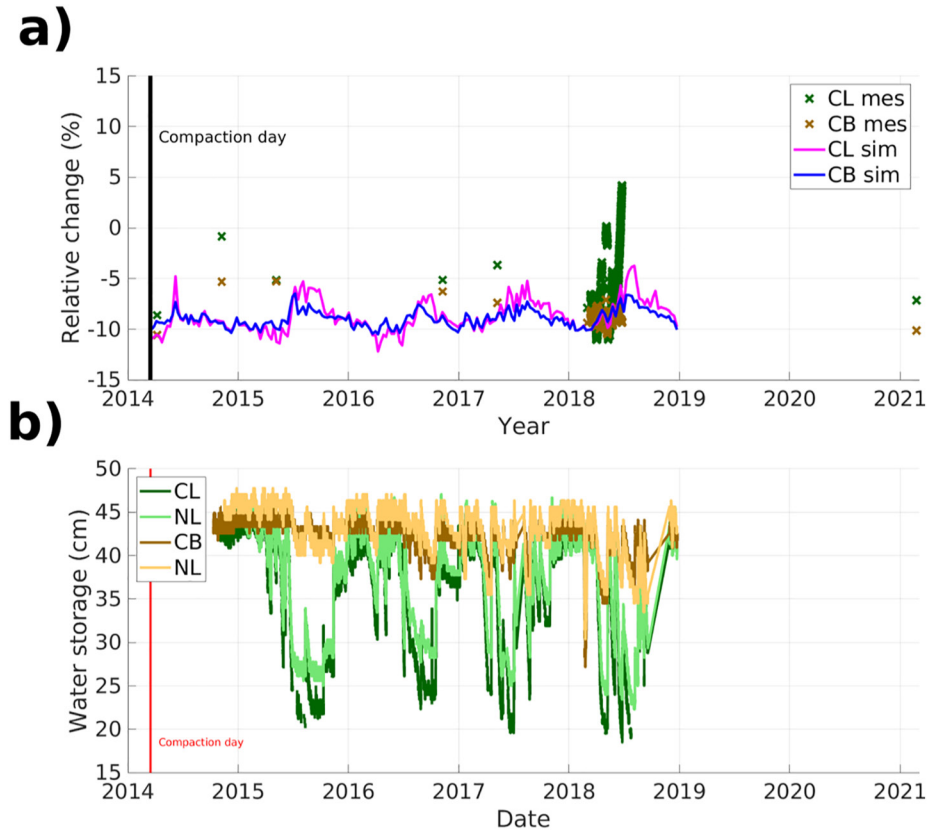

Figure 10. (a) Measured (mes) and simulated (sim) relative change in apparent electrical resistivity (Wenner array with 1 m spacing) for compacted and non-compacted ley (CL) and bare soil (CB). (b) Water storage calculated from TDR data for compacted ley (CL), non-compacted ley (NL), compacted bare soil (CB), and non-compacted bare soil (NB).

monitored period (Section 5.2.1). The relative differences from 2018 to 2021 remain similar to those measured shortly after the compaction event (about 10% decrease). An up to 10% decrease in apparent resistivity was captured by long-term simulations of apparent resistivity (Wenner array with 1 m spacing from 2013 to 2019) using the electrical properties inferred for 2018 (Figure 10). The 10% differences are mostly seen during wet periods (e.g., winter months) and are masked during drier periods (e.g., during spring and summer) due to the larger differences in water content of compacted and non-compacted soils.

6. Discussion

6.1. Influence of Soil Structure in Soil Moisture and Electrical Resistivity Dynamics

For the bare soil, the differences in measured soil water dynamics associated with soil compaction (compacted and non-compacted) were insufficient to produce distinguishing changes in the monitored apparent resistivities. The data followed a temperature-driven trend decreasing from the winter to the summer. The simulations are able to reproduce this trend with some discrepancies. They can be associated to the parameters of the model used to correct temperature effects (Campbell et al., 1948) in electrical resistivity that were not calibrated for this study; and to the slight mismatch in predictions and observations of water content and temperature. This occurs for both the bare soil and ley. For the bare soil, some discrepancies during the growing season might be attributed to overestimation of water losses in Part I of our modeling scheme for the bare soil (see Figure 2) and to variations in the electrical conductivity of soil water which are not accounted for in our pedophysical model. During the monitoring period (spring and summer), water flow occurred in the soil matrix and macropore activation (saturation of macropores) did not occur. For this reason, we did not identify a strong effect of macropore activation in the measured and modeled water contents and the related geoelectrical signal.

Due to the presence of vegetation in the ley soil, we observed a larger influence of soil compaction on soil water dynamics (Figure 4). The simulated differences in dynamics of electrical resistivity between compacted ley compared to non-compacted ley had slight discrepancies with observations during dry periods. During long dry periods, the simulated apparent resistivities of compacted ley remained lower than for non-compacted ley (see Figures 7c and 7d). The differences in simulated apparent resistivities of compacted and non-compacted ley, however, diminished considerably during dry periods. This is consistent with our observations, in which apparent resistivities of compacted ley switches to higher values than for non-compacted ley during dry periods. The discrepancy in simulated and observed apparent resistivity is attributed to the previously discussed underprediction of the differences in water storage of compacted ley relative to non-compacted ley (Figures 7a and 7b). Our modeling results suggest that the main process explaining differences in water content dynamics between compacted and non-compacted ley was soil evaporation. Similarly to the bare soil, we did not observe a major influence of macropore activation in the simulated water content and electrical signatures.

Our modeling-based approach employs modeled water contents as fixed input for the inverse modeling of apparent resistivity data. While differences in apparent resistivities between soil compaction treatments were qualitatively reproduced, the exact values were not properly matched by the modeling approach. These errors in reproducing the water content adversely affected the ability of the electrical model to reproduce the apparent resistivity data and possibly translated into errors in the electrical properties inferred by inverse modeling. The apparent resistivity data were better fitted using the interpolation-based approach (WRMSE = 0.76, using 10% data error) presented in the Section S1 in Supporting Information S1 than when using the modeling-based approach (WRMSE = 1.25). Both approaches led to lower values of M_{soil} for compacted versus non-compacted soils. Despite its less satisfactory performance in reproducing the electrical resistivity data, the modeling-based approach offers mechanistic understanding of soil structure-driven water content dynamics (in terms of enhanced evaporation rates). When TDR data are available, the interpolation-based approach is preferred for a rapid assessment of soil electrical properties in terms of compaction effects.

The measured and simulated water fluxes presented in Section 5.1.2 suggest that soil compaction produces a noticeable increase of soil surface evaporation from both unvegetated and vegetated soils. In the bare soil, enhanced soil surface evaporation due to compaction can be linked to the soil critical water content (Equation 11) that limits soil water losses and is higher for non-compacted bare soil (θ_{crit} = 0.35 $cm^3\,cm^{-3}$ versus θ_{crit} = 0.33 $cm^3\,cm^{-3}$). In the ley soil, differences in water losses in compacted and non-compacted soils are larger and more difficult to explain, partly due to the presence of vegetation. The higher aboveground biomass in the non-compacted ley compared to the compacted ley suggest that, similarly to the bare soil, water losses in the compacted ley are produced by enhanced soil evaporation capabilities. Our modeling approach makes it possible to interpret this effect by considering an increase in the soil characteristic evaporation depth resulting from soil compaction. Our observations and modeling suggest that soil compaction might have a large impact on soil-atmosphere water partition due to a considerable enhancement of evaporative fluxes. This topic merits further and more detailed investigation.

6.2. Soil Compaction Effects Revealed by Geoelectrical Data

Compacted soils at the SSO have lower apparent electrical resistivities than non-compacted soils for the same soil water storage (Figure 4). Lower resistivities in compacted soils have been widely reported in the literature (e.g., Besson et al., 2013; Séger et al., 2009). Four years after the prescribed compaction, we observed up to a 11% decrease in apparent electrical resistivity in compacted soils (Figure 10). This is similar to the change in inverted electrical resistivity of compacted treatments a few days after compaction compared with their precompaction states reported by Keller et al. (2017). In addition, long-term effects of compaction in geoelectrical data presented in Figure 10 suggest a limited recovery of the compacted soils. We suggest that detecting soil compaction with geoelectrical methods might be best achieved outside the growing seasons (i.e., when evapotranspiration is negligible) at times when the water content is high.

We used inverse modeling of electrical properties for interpreting the observed differences in apparent resistivities by modeling and inferring electrical properties that are distinctive of the compaction treatments (w_{mac} and M_{soil}) and electrical properties that are common for all experimental plots (σ_s, σ_w, and m_{sm}). This assumption was made based on the extensive literature suggesting that soil compaction impacts primarily the interaggregate pore spaces (macropores) and aggregate contacts (Berli et al., 2008; Eggers et al., 2006; Ghezzehei & Or, 2000, 2001;

Or & Ghezzehei, 2002). The macroporosity (w_{mac}) was calculated based on saturated hydraulic conductivity data (see Section 4.2) and the exponent M_{soil} was inferred from the inversion (see Section 4.3) and is the only fitting parameter for differentiating compacted and non-compacted soils. The inferred posteriors of M_{soil} revealed lower values for compacted soils than for non-compacted soils, with mean values of 2.3 and 4.2, respectively. The difference between M_{soil} of compacted and non-compacted soils is consistently negative as shown in Figures 9b and 9c. Similar values are obtained when using the interpolation-based approach (Section S1 in Supporting Information S1) resulting in mean values of 2.6 and 3.9 for compacted and non-compacted soils, respectively. This indicates that the prescribed differences in macroporosity are insufficient to describe the lower electrical resistivity observed in compacted soils (see e.g., Figure 1c).

Assuming that differences in macroporosity are correctly inferred, this implies an increase of connectivity of soil aggregates as a result of soil compaction (see also Cimpoiasu et al., 2021). Such increases in aggregate connectivity for compacted soils are predicted when studying the dynamics of soil aggregate contacts in response to compaction controlled by soil rheology (see e.g., Or & Ghezzehei, 2002). Similar effects have been observed for hydraulic properties of partially saturated soils. For instance, Carminati et al. (2007) showed that hydraulic conductivity increases with increasing hydraulic contacts between soil grains. A similar result was observed for soil seismic properties at the SSO by Romero-Ruiz et al. (2021). Therein, the differences in seismic velocities (strongly sensitive to mechanical resistance of soils) of compacted and non-compacted soils were interpreted in terms of the contact area between soil aggregates. In Section S2 in Supporting Information S1, we present how varying both w_{mac} and M_{soil} leads to negatively correlated posterior estimates and the recognition that the inversion alone cannot distinguish between the two parameters. Clearly, both properties are important and the effects of soil compaction cannot only be explained by an increase in aggregate connectivity.

6.3. Limitations

This work offers new insights into the electrical signatures of soil water dynamics in structured soils by expressing how key soil structural features vary with space and time. Nevertheless, a few important elements were omitted from consideration that appear to be important for consideration in future studies. For example, the electrical conductivity of water is varying with time and will impact electrical monitoring data (Coscia et al., 2012). However, the dynamics of these changes in salinity are expected to be similar in all experimental plots. Other effects may include the spatial heterogeneity of soil properties. This may impact the electrical properties as a function of soil depth and this is not considered in this work. Here, the focus was on capturing differences between compacted and non-compacted soils and only variations of macroporosity and saturated hydraulic conductivity with soil depth were considered. In addition, it is expected that macroporosities, mesoporosities, and microporosities change not only as a function of depth but also as a function of time in response to biological activity, climatic cycles and management. Such pore-space changes produce concurrent changes in soil hydraulic properties and associated geophysical responses. Ideally, this should be formally considered when modeling soil processes. For example, frameworks that consider pore-space dynamics (e.g., Meurer et al., 2020; Stewart et al., 2016) may be extended to incorporate changes in soil hydraulic and geophysical properties for integration in soil process modeling. Despite the missing elements highlighted here, our works offers a way forward to advance understanding and monitoring capabilities of soil hydrological processes strongly influenced soil structural features by integrating hydrologeophysical modeling and monitoring.

7. Conclusions

We developed a coupled hydrogeophysical modeling scheme to study the influence of soil structure on soil water content and electrical resistivity dynamics and enhance our monitoring capabilities at the plot scale. This modeling scheme consistently accounts for soil structure effects on soil electrical, hydraulic and evaporation properties. It includes a new pedophysical model to interpret electrical properties of structured soils in terms of macroporosity and connectivity of soil aggregates. The modeling scheme was used to analyze DC-resistivity monitoring data from a soil compaction experiment. The apparent electrical resistivity data revealed that compacted soils are less resistive than non-compacted soils when comparing the two at the same water content. We found that macroporosity and the connectivity of soil aggregates are negatively correlated and that geoelectrical data can be reproduced to similar levels over a rather wide range of values of their related parameters. By constraining values of macroporosity with observations of saturated hydraulic conductivity, we attribute the observed

lower electrical resistivity of compacted soils to a decrease in macroporosity and partly to an increase in connectivity among soil aggregates. Higher water losses in compacted compared with non-compacted soil could be reproduced qualitatively by considering a larger evaporation length and lower critical water content for Stage-I evaporation in compacted soil. We stress that the partition of soil water in compacted vegetated soils deserves further investigation. The proposed modeling scheme expands our ability to capture and interpret geoelectrical signatures of soil structure. It provides insights of how small differences in soil physical properties may induce significant changes in soil-atmosphere water (and energy) fluxes. By illustrating impacts of soil compaction on soil water dynamics at the plot scale, the results suggest that considering soil structure impacts on water dynamics could improve predictions of Earth system models.

Data Availability Statement

The geophysical data used in this study are available at (Romero-Ruiz, 2021; https://doi.org/10.5281/zenodo.5781234).

Acknowledgments
The authors are grateful to Peter Lehmann (ETH-Zürich) for useful discussions on soil-specific evaporation models. Viktor Stadelmann, Valerio Volpe, and Rebecca Schneiter (Agroscope) are thanked for their help with logistics at the SSO. We are thankful for the insightful comments offered by associate editor Andrew Binley, Sarah Garré and two anonymous reviewers.

References

Annan, A. P. (2005). GPR methods for hydrogeological studies. In Y. Rubin & S. S. Hubbard (Eds.), *Hydrogeophysics* (pp. 185–213). Dordrecht: Springer. https://doi.org/10.1007/1-4020-3102-5_7

Aravena, J. E., Berli, M., Ruiz, S., Suárez, F., Ghezzehei, T. A., & Tyler, S. W. (2014). Quantifying coupled deformation and water flow in the rhizosphere using X-ray microtomography and numerical simulations. *Plant and Soil*, *376*(1), 95–110. https://doi.org/10.1007/s11104-013-1946-z

Araya, S. N., & Ghezzehei, T. A. (2019). Using machine learning for prediction of saturated hydraulic conductivity and its sensitivity to soil structural perturbations. *Water Resources Research*, *55*, 5715–5737. https://doi.org/10.1029/2018WR024357

Archie, G. E. (1942). The electrical resistivity log as an aid in determining some reservoir characteristics. *Transactions of the AIME*, *146*(1), 54–62. https://doi.org/10.2118/942054-G

Assouline, S., Narkis, K., Gherabli, R., Lefort, P., & Prat, M. (2014). Analysis of the impact of surface layer properties on evaporation from porous systems using column experiments and modified definition of characteristic length. *Water Resources Research*, *50*, 3933–3955. https://doi.org/10.1002/2013WR014489

Bengough, A. G., McKenzie, B. M., Hallett, P. D., & Valentine, T. A. (2011). Root elongation, water stress, and mechanical impedance: A review of limiting stresses and beneficial root tip traits. *Journal of Experimental Botany*, *62*(1), 59–68. https://doi.org/10.1093/jxb/erq350

Berli, M., Accorsi, M. L., & Or, D. (2006). Size and shape evolution of pores in a viscoplastic matrix under compression. *International Journal for Numerical and Analytical Methods in Geomechanics*, *30*(12), 1259–1281. https://doi.org/10.1002/nag.529

Berli, M., Carminati, A., Ghezzehei, T. A., & Or, D. (2008). Evolution of unsaturated hydraulic conductivity of aggregated soils due to compressive forces. *Water Resources Research*, *44*, W00C09. https://doi.org/10.1029/2007WR006501

Besson, A., Séger, M., Giot, G., & Cousin, I. (2013). Identifying the characteristic scales of soil structural recovery after compaction from three in-field methods of monitoring. *Geoderma*, *204*, 130–139. https://doi.org/10.1016/j.geoderma.2013.04.010

Binley, A., Hubbard, S. S., Huisman, J. A., Revil, A., Robinson, D. A., Singha, K., & Slater, L. (2015). The emergence of hydrogeophysics for improved understanding of subsurface processes over multiple scales. *Water Resources Research*, *51*, 3837–3866. https://doi.org/10.1002/2015WR017016

Binley, A., & Kemna, A. (2005). DC resistivity and induced polarization methods. In Y. Rubin & S. S. Hubbard (Eds.), *Hydrogeophysics* (pp. 129–156). Dordrecht:Springer. https://doi.org/10.1007/1-4020-3102-5_5

Binley, A., & Slater, L. (2020). *Resistivity and induced polarization: Theory and applications to the near-surface Earth*. Cambridge University Press.

Blanchy, G., Watts, C. W., Richards, J., Bussell, J., Huntenburg, K., Sparkes, D. L., et al. (2020). Time-lapse geophysical assessment of agricultural practices on soil moisture dynamics. *Vadose Zone Journal*, *19*(1), e20080. https://doi.org/10.1002/vzj2.20080

Blonquist Jr, J., Jones, S. B., Lebron, I., & Robinson, D. (2006). Microstructural and phase configurational effects determining water content: Dielectric relationships of aggregated porous media. *Water Resources Research*, *42*, W05424. https://doi.org/10.1029/2005WR004418

Bonetti, S., Wei, Z., & Or, D. (2021). A framework for quantifying hydrologic effects of soil structure across scales. *Communications Earth & Environment*, *2*(1), 1–10. https://doi.org/10.1038/s43247-021-00180-0

Bottinelli, N., Jouquet, P., Capowiez, Y., Podwojewski, P., Grimaldi, M., & Peng, X. (2015). Why is the influence of soil macrofauna on soil structure only considered by soil ecologists? *Soil and Tillage Research*, *146*(A), 118–124. https://doi.org/10.1016/j.still.2014.01.007

Bussian, A. E. (1983). Electrical conductance in a porous medium. *Geophysics*, *48*(9), 1258–1268. https://doi.org/10.1190/1.1441549

Campbell, R. B., Bower, C. A., & Richards, L. A. (1948). Change of electrical conductivity with temperature and the relation of osmotic pressure to electrical conductivity and ion concentration for soil extracts. In *Soil Science Society of America Proceedings* (Vol. 13, pp. 66–69).

Carminati, A., Kaestner, A., Flühler, H., Lehmann, P., Or, D., Lehmann, E., & Stampanoni, M. (2007). Hydraulic contacts controlling water flow across porous grains. *Physical Review E—Statistical Physics, Plasmas, Fluids, and Related Interdisciplinary Topics*, *76*, 026311. https://doi.org/10.1103/PhysRevE.76.026311

Carsel, R. F., & Parrish, R. S. (1988). Developing joint probability distributions of soil water retention characteristics. *Water Resources Research*, *24*(5), 755–769. https://doi.org/10.1029/WR024i005p00755

Cimpoiasu, M. O., Kuras, O., Wilkinson, P. B., Pridmore, T., & Mooney, S. J. (2021). Hydrodynamic characterization of soil compaction using integrated electrical resistivity and X-ray computed tomography. *Vadose Zone Journal*, *20*, 1–15. https://doi.org/10.1002/vzj2.20109

Colombi, T., Braun, S., Keller, T., & Walter, A. (2017). Artificial macropores attract crop roots and enhance plant productivity on compacted soils. *The Science of the Total Environment*, *574*, 1283–1293. https://doi.org/10.1016/j.scitotenv.2016.07.194

Coscia, I., Linde, N., Greenhalgh, S., Vogt, T., & Green, A. (2012). Estimating traveltimes and groundwater flow patterns using 3d time-lapse crosshole ert imaging of electrical resistivity fluctuations induced by infiltrating river water. *Geophysics*, *77*(4), E239–E250. https://doi.org/10.1190/geo2011-0328.1

Cosenza, P., Ghorbani, A., Camerlynck, C., Rejiba, F., Guérin, R., & Tabbagh, A. (2009). Effective medium theories for modelling the relationships between electromagnetic properties and hydrological variables in geomaterials: A review. *Near Surface Geophysics*, *7*(5–6), 563–578. https://doi.org/10.3997/1873-0604.2009009

Day-Lewis, F., Linde, N., Haggerty, R., Singha, K., & Briggs, M. A. (2017). Pore network modeling of the electrical signature of solute transport in dual-domain media. *Geophysical Research Letters*, *44*, 4908–4916. https://doi.org/10.1002/2017GL073326

De Vries, D. A. (1963). Thermal properties of soils. In W. R. Van Wijk (Ed.), *Physics of plant environment* (pp. 210–235). Amsterdam:North-Holland Publ. Co.

Dexter, A. (1988). Advances in characterization of soil structure. *Soil and Tillage Research*, *11*(3–4), 199–238. https://doi.org/10.1016/0167-1987(88)90002-5

Doolittle, J. A., & Brevik, E. C. (2014). The use of electromagnetic induction techniques in soils studies. *Geoderma*, *223*, 33–45. https://doi.org/10.1016/j.geoderma.2014.01.027

Durner, W. (1994). Hydraulic conductivity estimation for soils with heterogeneous pore structure. *Water Resources Research*, *30*(2), 211–223. https://doi.org/10.1029/93WR02676

Dvorkin, J., Prasad, M., Sakai, A., & Lavoie, D. (1999). Elasticity of marine sediments: Rock physics modeling. *Geophysical Research Letters*, *26*(12), 1781–1784. https://doi.org/10.1029/1999GL900332

Eggers, C. G., Berli, M., Accorsi, M. L., & Or, D. (2006). Deformation and permeability of aggregated soft earth materials. *Journal of Geophysical Research*, *111*, B10204. https://doi.org/10.1029/2005JB004123

Evans, S. (1965). Dielectric properties of ice and snow—A review. *Journal of Glaciology*, *5*(42), 773–792. https://doi.org/10.3189/S0022143000018840

Farahani, E., Emami, H., & Keller, T. (2018). Impact of monovalent cations on soil structure. Part II: Results of two Swiss soils. *International Agrophysics*, *32*(1), 69–80. https://doi.org/10.1515/intag-2016-0092

Fatichi, S., Or, D., Walko, R., Vereecken, H., Young, M. H., Ghezzehei, T. A., et al. (2020). Soil structure is an important omission in Earth System Models. *Nature Communications*, *11*(1), 1–11. https://doi.org/10.1038/s41467-020-14411-z

Feddes, R. (1978). Simulation of field water use and crop yield. In F. Penning de Vries & H. van Laar (Eds.), *Simulation of plant growth and crop production* (pp. 194–209). Pudoc.

Friedman, S. P. (2005). Soil properties influencing apparent electrical conductivity: A review. *Computers and Electronics in Agriculture*, *46*(1–3), 45–70. https://doi.org/10.1016/j.compag.2004.11.001

Garré, S., Hyndman, D., Mary, B., & Werban, U. (2021). Geophysics conquering new territories: The rise of "agrogeophysics". *Vadose Zone Journal*, *20*, e20115. https://doi.org/10.1002/vzj2.20115

Gelman, A., & Rubin, D. B. (1992). Inference from iterative simulation using multiple sequences. *Statistical Science*, *7*(4), 457–472. https://doi.org/10.1214/ss/1177011136

Gerke, H. H., Germann, P., & Nieber, J. (2010). Preferential and unstable flow: From the pore to the catchment scale. *Vadose Zone Journal*, *9*(2), 207–212. https://doi.org/10.2136/vzj2010.0059

Ghezzehei, T. A., & Or, D. (2000). Dynamics of soil aggregate coalescence governed by capillary and rheological processes. *Water Resources Research*, *36*(2), 367–379. https://doi.org/10.1029/1999WR900316

Ghezzehei, T. A., & Or, D. (2001). Rheological properties of wet soils and clays under steady and oscillatory stresses. *Soil Science Society of America Journal*, *65*(3), 624–637. https://doi.org/10.2136/sssaj2001.653624x

Glover, P. (2009). What is the cementation exponent? A new interpretation. *The Leading Edge*, *28*(1), 82–85. https://doi.org/10.1190/1.3064150

Glover, P., Hole, M. J., & Pous, J. (2000). A modified Archie's law for two conducting phases. *Earth and Planetary Science Letters*, *180*(3–4), 369–383. https://doi.org/10.1016/s0012-821x(00)00168-0

Hamza, M. A., & Anderson, W. K. (2005). Soil compaction in cropping systems: A review of the nature, causes and possible solutions. *Soil and Tillage Research*, *82*(2), 121–145. https://doi.org/10.1016/j.still.2004.08.009

Hanks, R. J. (2012). *Applied soil physics: Soil water and temperature applications* (Vol. 8). Springer Science & Business Media.

Hobley, E. U., & Wilson, B. (2016). The depth distribution of organic carbon in the soils of eastern Australia. *Ecosphere*, *7*(1), e01214. https://doi.org/10.1002/ecs2.1214

Ingeman-Nielsen, T., & Baumgartner, F. (2006). CR1Dmod: A Matlab program to model 1D complex resistivity effects in electrical and electromagnetic surveys. *Computers & Geosciences*, *32*(9), 1411–1419. https://doi.org/10.1016/j.cageo.2006.01.001

Jarvis, N., Koestel, J., & Larsbo, M. (2016). Understanding preferential flow in the vadose zone: Recent advances and future prospects from pore to catchment scales. *Vadose Zone Journal*, *15*(12), vzj2016.09.0075. https://doi.org/10.2136/vzj2016.09.0075

Jensen, M. E., & Haise, H. R. (1963). Estimating evapotranspiration from solar radiation. *Journal of the Irrigation and Drainage Division*, *89*, 15–41. https://doi.org/10.1061/jrcea4.0000287

Keller, T., Colombi, T., Ruiz, S., Manalili, M. P., Rek, J., Stadelmann, V., et al. (2017). Long-term Soil Structure Observatory for monitoring post-compaction evolution of soil structure. *Vadose Zone Journal*, *16*(4), vzj2016.11.0118. https://doi.org/10.2136/vzj2016.11.0118

Keller, T., Colombi, T., Ruiz, S., Schymanski, S. J., Weisskopf, P., Koestel, J., et al. (2021). Soil structure recovery following compaction: Short-term evolution of soil physical properties in a loamy soil. *Soil Science Society of America Journal*, *85*(4), 1002–1020. https://doi.org/10.1002/saj2.20240

Kowalsky, M. B., Finsterle, S., & Rubin, Y. (2004). Estimating flow parameter distributions using ground-penetrating radar and hydrological measurements during transient flow in the vadose zone. *Advances in Water Resources*, *27*(6), 583–599. https://doi.org/10.1016/j.advwatres.2004.03.003

Kramer, C., & Gleixner, G. (2008). Soil organic matter in soil depth profiles: Distinct carbon preferences of microbial groups during carbon transformation. *Soil Biology and Biochemistry*, *40*(2), 425–433. https://doi.org/10.1016/j.soilbio.2007.09.016

Laloy, E., & Vrugt, J. A. (2012). High-dimensional posterior exploration of hydrologic models using multiple-try DREAM(ZS) and high-performance computing. *Water Resources Research*, *48*, W01526. https://doi.org/10.1029/2011WR010608

Lehmann, P., Assouline, S., & Or, D. (2008). Characteristic lengths affecting evaporative drying of porous media. *Physical Review E*, *77*(5), 056309. https://doi.org/10.1103/physreve.77.056309

Lehmann, P., Berli, M., Koonce, J. E., & Or, D. (2019). Surface evaporation in arid regions: Insights from lysimeter decadal record and global application of a surface evaporation capacitor (SEC) model. *Geophysical Research Letters*, *46*, 9648–9657. https://doi.org/10.1029/2019GL083932

Lehmann, P., Bickel, S., Wei, Z., & Or, D. (2020). Physical constraints for improved soil hydraulic parameter estimation by pedotransfer functions. *Water Resources Research*, *56*, e2019WR025963. https://doi.org/10.1029/2019WR025963

Lesmes, D., & Friedman, S. (2005). Relationships between the electrical and hydrogeological properties of the rocks and soils. In Y. Rubin & S. S. Hubbard (Eds.), *Hydrogeophysics* (pp. 391–412). Springer.

Linde, N., Binley, A., Tryggvason, A., Pedersen, L. B., & Revil, A. (2006). Improved hydrogeophysical characterization using joint inversion of cross-hole electrical resistance and ground-penetrating radar traveltime data. *Water Resources Research*, *42*, W12404. https://doi.org/10.1029/2006WR005131

Meurer, K., Barron, J., Chenu, C., Coucheney, E., Fielding, M., Hallett, P., et al. (2020). A framework for modelling soil structure dynamics induced by biological activity. *Global Change Biology*, *26*(10), 5382–5403. https://doi.org/10.1111/gcb.15289

Moysey, S. M. J., & Liu, Z. (2012). Can the onset of macropore flow be detected using electrical resistivity measurements? *Soil Science Society of America Journal*, *76*(1), 10–17. https://doi.org/10.2136/sssaj2010.0413

Oades, J. M. (1993). The role of biology in the formation, stabilization and degradation of soil structure. *Geoderma*, *56*, 377–400. https://doi.org/10.1016/0016-7061(93)90123-3

Or, D., & Ghezzehei, T. A. (2002). Modeling post-tillage soil structural dynamics: A review. *Soil and Tillage Research*, *64*(1–2), 41–59. https://doi.org/10.1016/S0167-1987(01)00256-2

Or, D., & Lehmann, P. (2019). Surface evaporative capacitance: How soil type and rainfall characteristics affect global-scale surface evaporation. *Water Resources Research*, *55*, 519–539. https://doi.org/10.1029/2018WR024050

Or, D., Lehmann, P., Shahraeeni, E., & Shokri, N. (2013). Advances in soil evaporation physics—A Review. *Vadose Zone Journal*, *12*(4), vzj2012.0163. https://doi.org/10.2136/vzj2012.0163

Parker, R. L. (1984). The inverse problem of resistivity sounding. *Geophysics*, *49*(12), 2143–2158. https://doi.org/10.1190/1.1441630

Revil, A., Coperey, A., Shao, Z., Florsch, N., Fabricius, I., Deng, Y., et al. (2017). Complex conductivity of soils. *Water Resources Research*, *53*, 7121–7147. https://doi.org/10.1002/2017WR020655

Richards, L. A. (1931). Capillary conduction of liquids through porous mediums. *Physics*, *1*(5), 318–333. https://doi.org/10.1063/1.1745010

Romero-Ruiz, A. (2021). Geophysical data from: "Lasting effects of soil compaction on soil water regime confirmed by geoelectrical monitoring". *Zenodo*. https://doi.org/10.5281/zenodo.5781234

Romero-Ruiz, A., Linde, N., Baron, L., Solazzi, S. G., Keller, T., & Or, D. (2021). Seismic signatures reveal persistence of soil compaction. *Vadose Zone Journal*, *20*, e20140. https://doi.org/10.1002/vzj2.20140

Romero-Ruiz, A., Linde, N., Keller, T., & Or, D. (2018). A review of geophysical methods for soil structure characterization. *Reviews of Geophysics*, *56*, 672–697. https://doi.org/10.1029/2018RG000611

Roth, K., Schulin, R., Fluhler, H., & Attinger, W. (1990). Calibration of Time Domain Reflectometry for water content measurement using a composite dielectric approach. *Water Resources Research*, *26*(10), 2267–2273. https://doi.org/10.1029/WR026i010p02267

Séger, M., Cousin, I., Frison, A., Boizard, H., & Richard, G. (2009). Characterisation of the structural heterogeneity of the soil tilled layer by using in situ 2D and 3D electrical resistivity measurements. *Soil and Tillage Research*, *103*(2), 387–398. https://doi.org/10.1016/j.still.2008.12.003

Seladji, S., Cosenza, P., Tabbagh, A., Ranger, J., & Richard, G. (2010). The effect of compaction on soil electrical resistivity: A laboratory investigation. *European Journal of Soil Science*, *61*(6), 1043–1055. https://doi.org/10.1111/j.1365-2389.2010.01309.x

Simunek, J., Šejna, M., Saito, H., Sakai, M., & Genuchten, M. T. V. (2013). *The HYDRUS-1D software Package for simulating the movement of water, heat, and multiple solutes in variably saturated media, Version 4.17, HYDRUS Software Series* (Vol. 3, pp. 343).

Sophocleous, M. (1979). Analysis of water and heat flow in unsaturated-saturated porous media. *Water Resources Research*, *15*(5), 1195–1206. https://doi.org/10.1029/WR015i005p01195

Steduto, P., Hsiao, T. C., & Fereres, E. (2007). On the conservative behavior of biomass water productivity. *Irrigation Science*, *25*(3), 189–207. https://doi.org/10.1007/s00271-007-0064-1

Stewart, R. D., Rupp, D. E., Abou Najm, M. R., & Selker, J. S. (2016). A unified model for soil Shrinkage, Subsidence,and Cracking. *Vadose Zone Journal*, *15*(3), vzj2015.11.0146. https://doi.org/10.2136/vzj2015.11.0146

Tran, A. P., Dafflon, B., & Hubbard, S. S. (2017). Coupled land surface-subsurface hydrogeophysical inverse modeling to estimate soil organic carbon content and explore associated hydrological and thermal dynamics in the Arctic tundra, *The Cryosphere*, *11*, 2089–2109. https://doi.org/10.5194/tc-11-2089-2017

van Genuchten, M. T. (1980). A closed-form equation for predicting the hydraulic conductivity of unsaturated soils1. *Soil Science Society of America Journal*, *44*(5), 892, 898. https://doi.org/10.2136/sssaj1980.03615995004400050002x

van Genuchten, M. T. (1987). *A numerical model for water and solute movement in and below the root zone* (Unpublished Research Report).

Van Looy, K., Bouma, J., Herbst, M., Koestel, J., Minasny, B., Mishra, U., et al. (2017). Pedotransfer functions in Earth system science: Challenges and perspectives. *Reviews of Geophysics*, *55*, 1199–1256. https://doi.org/10.1002/2017RG000581

Vereecken, H., Kasteel, R., & Harter, T. (2007). Upscaling hydraulic properties and soil water flow processes in heterogeneous soils. *Vadose Zone Journal*, *6*(1), 1–28. https://doi.org/10.2136/vzj2006.0055

von Hebel, C., Reynaert, S., Pauly, K., Janssens, P., Piccard, I., Vanderborght, J., et al. (2020). Toward high-resolution agronomic soil information and management zones delineated by ground-based electromagnetic induction and aerial drone data. *Vadose Zone Journal*, e20099. https://doi.org/10.1002/vzj2.20099

Waxman, M. H., & Smits, L. J. M. (1968). Electrical conductivities in oil-bearing shaly sands. *Society of Petroleum Engineers Journal*, *8*(2), 107–122. https://doi.org/10.2118/1863-A

Weast, R. C., Astle, M. J., & Beyer, W. H. (1988). *CRC Handbook of Chemistry and Physics* (Vol. 69). CRC Press.

Zuo, Q., Shi, J., Li, Y., & Zhang, R. (2006). Root length density and water uptake distributions of winter wheat under sub-irrigation. *Plant and Soil*, *285*(1/2), 45–55. https://doi.org/10.1007/s11104-005-4827-2